Sensors & Actuators: A. Physical 362 (2023) 114639

Contents lists available at ScienceDirect

Sensors and Actuators: A. Physical

journal homepage: www.journals.elsevier.com/sensors-and-actuators-a-physical

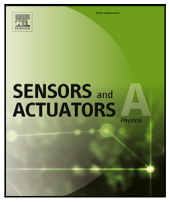

Analytical and experimental study of stress effects in a MEMS ring gyroscope

Mehran Hosseini-Pishrobat [a,*], Derin Erkan [a], Erdinc Tatar [a,b]

[a] Department of Electrical and Electronics Engineering, Bilkent University, Ankara, 06800, Turkey
[b] National Nanotechnology Research Center (UNAM), Bilkent University, Ankara, 06800, Turkey

ARTICLE INFO

Keywords:
Extensible ring
Ring gyroscope
Stress sensing
Quadrature error
In-phase error

ABSTRACT

External stress affects the stiffness distribution of a MEMS gyroscope and, along with temperature, is affiliated with long-term drift. Although the detrimental effects of stress on MEMS gyroscopes are well-documented, modeling of such effects is still lacking in the literature. For the first time, we present an analytical model that mathematically describes the stress effects in a ring gyroscope. Our model revolves around the key observation that stress-induced anchor displacements result in variations of electrostatic gaps and nonhomogeneous boundary conditions at the interface between the gyroscope's suspension system and the anchored internal structure. Our gyroscope is equipped with 16 capacitive stress sensors distributed with 45° symmetry on the inside and outside of the main ring. We use these stress sensors' measurements to interpolate the strain field across the substrate and deduce the anchor displacements. To capture the stress effects, we show that two fundamental assumptions in the existing literature should be amended: *(1) Linearity:* the linear engineering strain should be upgraded to the nonlinear Green–Lagrange strain to reveal the stress-induced stiffness through geometric nonlinearity; *(2) Inextensibility:* for a ring, this stress stiffness is determined by the extensional stress arising from centerline extensibility. We analyze variations of frequencies and mode shapes' orientation along with the resultant quadrature and in-phase errors. Moreover, we present a fairly general formulation incorporating fabrication-induced imperfections and elastic anisotropy. We validate our model experimentally using extensive bending tests performed on our 59 kHz, 3.2 mm diameter gyroscope.

1. Introduction

Motivation. MEMS Coriolis vibratory gyroscopes-compared to mechanical and optical gyroscopes—offer competitive advantages such as small footprint size, low power consumption, and high production rates using well-established microfabrication technologies. Nonetheless, long-term drift is one of the long-standing obstacles that prevent MEMS gyroscopes from attaining navigation-grade performance. Based on the temperature-drift correlation, temperature calibration is the widely used drift compensation method in both industry and academic research [1–3]. It has been shown that stress is another contributing factor in the drift, and one can achieve a superior drift compensation using both stress and temperature [4]. Along the same line, the recent paper [5] demonstrated that a time-partitioned stress-based drift compensation could significantly improve the bias stability of a 57 kHz, 3.2 mm diameter vibrating ring gyroscope (VRG) from 0.7°/h to 0.008°/h. The connection established in [4,5] between stress and gyroscope performance is, in effect, a statistical correlation. Our goal in this paper is to examine and understand the impact of stress from a first-principle analytical modeling viewpoint. Our aspiration is that this approach has the potential to pave the way for online stress-based drift calibration. We expand upon the preliminary results reported in [6] concerning frequency variation and provide new experimental data.

Literature review. There has been a considerable effort in the MEMS gyroscope community to replicate the outstanding performance of the hemispherical resonator gyroscope (HRG) [7] using circularly symmetric structures such as rings and disks [8–12]. The precision shell integrating (PSI) gyroscope [13] with 0.0014°/h bias instability demonstrates a recent successful replication of HRG in 1 cm diameter. The circular symmetry of a mechanical structure endows its modal space with distinct pairs of frequency-matched orthogonal mode shapes. Therefore, the structure possesses the ideal vibrational characteristics required for a Coriolis-based operation, standing as a promising candidate for high-performance MEMS gyroscopes.

The adverse effects of stress in MEMS devices have been well-studied in the literature. Inertial MEMS sensors used in strapdown navigation applications are often subject to shock, external vibration, and cyclic mechanical loads that impose undesired stresses on the device [14]. The die attachment quality in the packaging process is, however, a more critical factor that gives rise to stress in a MEMS

* Corresponding author.
E-mail addresses: mehran@ee.bilkent.edu.tr (M. Hosseini-Pishrobat), derin@ee.bilkent.edu.tr (D. Erkan), etatar@ee.bilkent.edu.tr (E. Tatar).

https://doi.org/10.1016/j.sna.2023.114639
Received 26 May 2023; Received in revised form 17 August 2023; Accepted 4 September 2023
Available online 9 September 2023
0924-4247/© 2023 Elsevier B.V. All rights reserved.

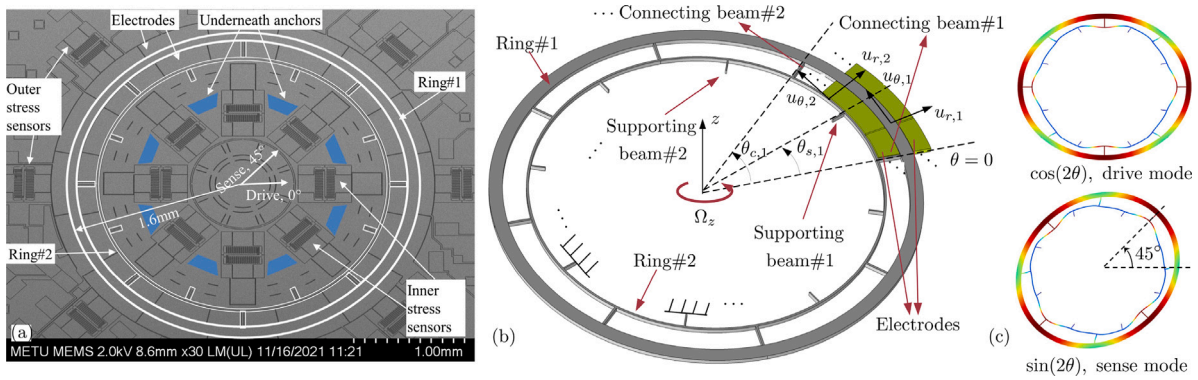

Fig. 1. Ring gyroscope's SEM (a), schematics (b), and $n = 2$ wineglass mode shapes (c).

Table 1
Key parameters of ring gyroscope.

Symbol	Definition	Value
R_1	Mean radius of Ring#1	1550 μm
R_2	Mean radius of Ring#2	1317 μm
w_1	Width of Ring#1	100 μm
w_2	Width of Ring#2	16 μm
l_c	Length of each connecting beam	175 μm
w_c	Width of each connecting beam	16 μm
l_s	Length of each supporting beam	110 μm
w_s	Width of each supporting beam	10 μm
g_0	Electrostatic gap	3.6 μm
h	Structural thickness	35 μm
ρ	Mass density	2329 kg/m^3
E	Young's modulus	170 GPa

device. The mismatch between the coefficients of thermal expansion of the MEMS die, the package substrate, and, if any, the gluing material could lead to residual and dynamic stresses as the device experiences abrupt temperature changes or undergoes thermal cycles [15]. One way to deal with this issue is to use modified, adhesive-free bonding techniques to minimize the packaging stress [16]. Another way is to apply a compensation algorithm using the data provided by deployed stress sensors [4]. The recent paper [17] showed that stress-based correction is remarkably effective in reducing humidity-related scale factor drifts of plastic packaged gyroscopes.

Compared to the commonly used finite element method (FEM), analytical modeling of MEMS gyroscopes can provide further insight into the underlying physics as a crucial step toward a thorough evaluation and enhancement of the devices' performance. For ring gyroscopes, analytical modeling has been used to analyze mismatches in mass and stiffness matrices [18], sensitivity to exogenous vibrations [19], fabrication-induced structural imperfection [20,21], and parametric excitation [22]. However, to the best of our knowledge, there has been very limited attempts on analytical modeling of stress effects. Apart from our initial results [6], the paper [23] reported a modeling procedure for the scale factor changes under one-dimensional PCB bending stresses, focusing on electrostatics as the determining factor.

Contribution. Fig. 1 shows the SEM and schematics of our 59 kHz, $n = 2$ wineglass modes VRG, and Table 1 summarizes its key parameters. The VRG has a double-ring structure with 16 beams and is equipped with 16 capacitive stress sensors. The device is fabricated from (111) wafers using a silicon-on-glass (SOG) process [24]. The main contribution of this paper is to lay out an analytical framework to model the effects of stress on frequencies, mode shape orientations, and quadrature/in-phase errors of this VRG. The key findings and novelty aspects of this framework are as follows.

- We present a solid mechanical formulation of rings and beams, the components of the gyroscope's mechanical structure, using Green–Lagrange strain to take geometric nonlinearity into account. Moreover, our formulation accommodates fabrication-induced (e.g., nonuniform etching, mask bias) imperfections and elastic anisotropy.
- The fundamental effect of stress on the gyroscope's structure is the displacement of anchors from their designated locations. In terms of modeling, these anchors displacements translate into
    1. Nonhomogeneous (i.e., nonzero) boundary conditions at the interface between the gyroscope's suspension and the internal anchored structure. In our gyroscope, the anchor displacements within the internal structure push/pull the eight supporting beams and, in turn, impose additional bending and extensional stresses on the inner ring. We show that the extensional component of these imposed stresses is the major contributor to the stiffness, and the inner ring's extensibility is necessary for its correct modeling.
    2. Variations of the electrostatic gap due to the displacements of anchored electrodes, which then alters the electrostatic softening.
- The stress sensors in our gyroscope provide us with the local radial strains at the substrate level. We use these measurements to interpolate the strain field across the substrate and then obtain the anchor displacements that determine the nonhomogeneous boundary conditions and the electrostatic gap variations.
- Our formulation shows that stress could affect both diagonal and off-diagonal entries of the gyroscope's stiffness matrix. We study the subsequent effects on the natural frequencies and quadrature/in-phase errors.

We performed extensive tests by applying bending loads on the gyroscope's die and recorded the stress sensors' outputs, frequency variations, and quadrature/in-phase errors. We also implemented our analytical model in a simulation setup that accepts the stress sensors' data as the input. Comparison between the experimental and simulation results for frequency shifts and quadrature/in-phase errors demonstrates the validity of our modeling.

Paper organization. Section 2 sets out the main results on the analytical modeling of stress effects. Section 3 explains the process for interpolating anchor displacements from the on-chip stress sensors' data. Section 4 uses the results of Section 2 to analyze the gyroscope's performance in terms of changes in vibrational properties and quadrature/in-phase errors. Section 5 presents the experimental results in comparison with the analytical model's predictions. Finally, Section 6 draws the concluding remarks.

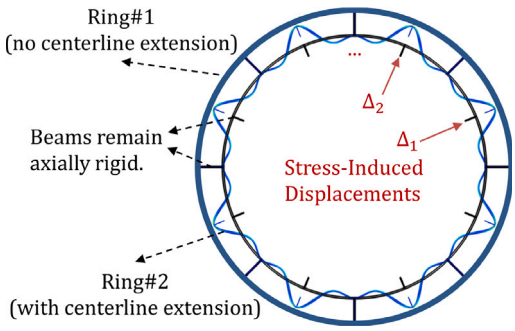

Fig. 2. Illustration of rings' extensibility under stress effects; the inner ring experiences extensibility while the outer rings remains unaffected.

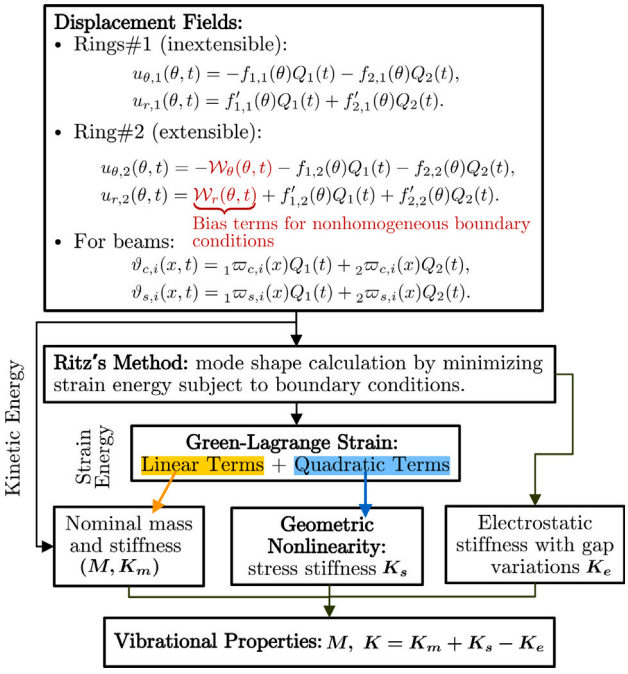

Fig. 3. Flowchart of main steps of analytical modeling.

2. Analytical modeling

2.1. Main idea

Our goal in this section is to mathematically model the link between stress at the substrate level and the subsequent changes in the stiffness matrix. As shown in Fig. 1(b), the VRG's mechanical structure comprises the following components: Ring#1 (outer ring), Ring#2 (inner ring), $4n$ connecting beams between the two rings, and $4n$ supporting beams that connect Ring#2 to the anchored internal structure. Here, $n = 2, 3, \ldots$ is the mode number. As illustrated by Fig. 2, Ring#2 takes up the load resulting from anchor displacements while Ring#1 remains unaffected. As a result, Ring#2 is subject to additional extensional stress besides the preexisting bending generated by the gyroscope's vibration. This key observation implies that we need to consider centerline extensibility only for Ring#2. The beams are all axially rigid, so they experience pure bending. In the structures that are under both axial and bending loads, second-order displacement-strain relations should be considered to fully characterize the stiffness [25]. We, therefore, adopt the Green–Lagrange strain to analyze Ring#2 and proceed with the usual linear strain for the rest of the structure. The flowchart in Fig. 3 explains the big picture of our modeling. The essence

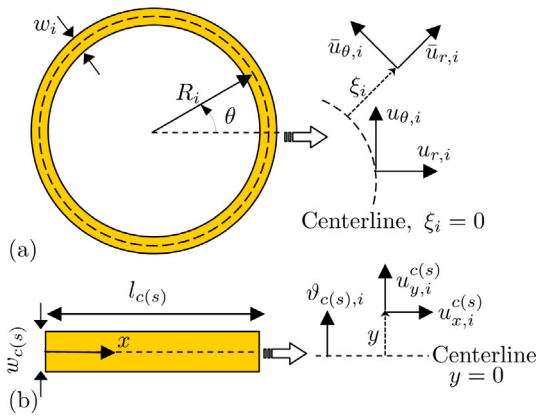

Fig. 4. Displacement fields of Ring#i (a) and connecting (supporting) beam#i (b).

of our method is to calculate the unknown mode shapes to have a complete description of the displacement fields, form the kinetic and strain energies, and finally obtain the mass and stiffness matrices.

2.2. Solid mechanics formulation

We use the cylindrical coordinate system $\{r, \theta, z\}$ as the gyroscope-fixed reference frame. Ring#i, $i = 1, 2$, has a fixed mean radius of R_i, but we allow a varying width, $w_i(\theta)$ to accommodate for possible geometric imperfections. In our formulation, such imperfections appear as variable area, $A_i(\theta)$ and second moment of area, $I_i(\theta)$ of the Ring#i's cross-section. Our analysis is based on the narrow ring assumption (i.e., $\max_{\theta\in[0,2\pi]} w_i(\theta)/R_i \ll 1$) and Euler–Bernoulli beam theory.

Rings. We introduce the coordinate ξ_i as the distance from the Ring#i's centerline and denote the displacement field at $\xi_i = 0$ by $\big(u_{r,i}(\theta,t), u_{\theta,i}(\theta,t)\big)$ with $t \geq 0$ being time (see Fig. 4(a)). For Ring#i, the rotation caused by bending of the cross-section located at the angle θ is given by [26]

$$\gamma_i(\theta,t) = \frac{1}{R_i}\left(u_{\theta,i}(\theta,t) - \frac{\partial u_{r,i}}{\partial\theta}(\theta,t)\right), \tag{1}$$

which has two components: rotation due to the tangential displacement (the first term) and rotation due to the gradient of the radial displacement around the cross-section (the second term). Following the Euler–Bernoulli beam theory, we obtain the displacement field $\big(\bar{u}_{r,i}(\xi_i,\theta,t), \bar{u}_{\theta,i}(\xi_i,\theta,t)\big)$ across Ring#i as

$$\begin{aligned}\bar{u}_{r,i}(\xi_i,\theta,t) &= u_{r,i}(\theta,t),\\ \bar{u}_{\theta,i}(\xi_i,\theta,t) &= u_{\theta,i}(\theta,t) + \xi_i\gamma_i(\theta,t).\end{aligned} \tag{2}$$

Based on Eq. (2), the extensional Green–Lagrange strain in Ring#i is

$$\mathcal{E}_{\theta\theta,i} = \varepsilon_{\theta\theta,i} + \eta_{\theta\theta,i}, \tag{3}$$

where $\varepsilon_{\theta\theta,i}$ and $\eta_{\theta\theta,i}$–the linear and nonlinear strain components, respectively–are given by

$$\begin{aligned}\varepsilon_{\theta\theta,i} &= \varepsilon_{0,i} + \xi_i\kappa_i,\\ \eta_{\theta\theta,i} &= \frac{1}{2}\left(\left(\varepsilon_{0,i} + \xi_i\kappa_i\right)^2 + \left(1 + \frac{\xi_i}{R_i}\right)^2\gamma_i^2\right).\end{aligned} \tag{4}$$

Here, $\varepsilon_{0,i}$ and κ_i are the centerline's extensional strain and curvature change, respectively:

$$\begin{aligned}\varepsilon_{0,i}(\theta,t) &= \frac{1}{R_i}\left(u_{r,i}(\theta,t) + \frac{\partial u_{\theta,i}}{\partial\theta}(\theta,t)\right),\\ \kappa_i(\theta,t) &= \frac{1}{R_i}\frac{\partial\gamma_i}{\partial\theta}(\theta,t) \approx \frac{1}{R_i + \Delta R_i} - \frac{1}{R_i}.\end{aligned} \tag{5}$$

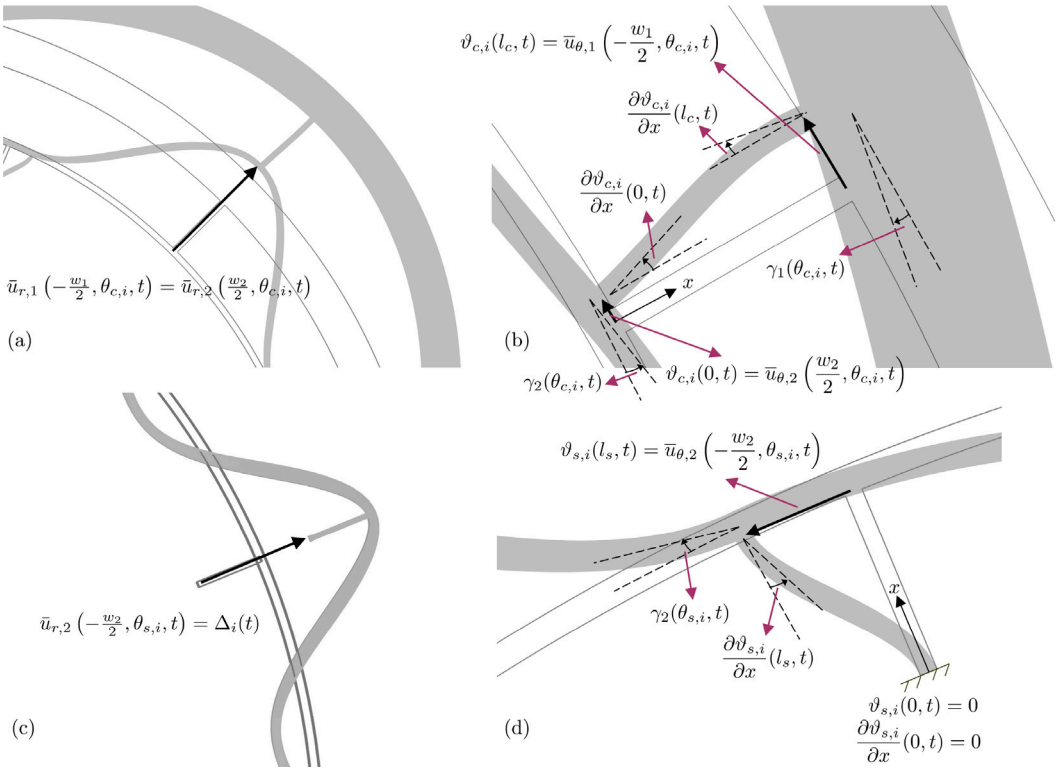

Fig. 5. Illustration of the boundary conditions of connecting beam#i ((a), (b)) and supporting beam#i ((c), (d)).

The calculation details of the Green–Lagrange strain tensor in the cylindrical coordinate system can be found in [27, Chapter 3]. Based on Eq. (3), the total strain energy in Ring#i is given by

$$\mathcal{U}_i = \mathcal{U}_i^L + \mathcal{U}_i^{NL}, \tag{6}$$

$$\mathcal{U}_i^L = \frac{1}{2}R_i h\int_0^{2\pi} E(\theta)\int_{-w_i(\theta)/2}^{w_i(\theta)/2}\varepsilon_{\theta\theta,i}^2(\xi_i,\theta,t)\mathrm{d}\xi_i\mathrm{d}\theta,$$

$$\mathcal{U}_i^{NL} = \frac{1}{2}R_i h\int_0^{2\pi} E(\theta)\int_{-w_i(\theta)/2}^{w_i(\theta)/2}\eta_{\theta\theta,i}^2(\xi_i,\theta,t) + 2\eta_{\theta\theta,i}(\xi_i,\theta,t)\varepsilon_{\theta\theta,i}(\xi_i,\theta,t)\mathrm{d}\xi_i\mathrm{d}\theta,$$

where $\mathcal{U}_i^L$ and $\mathcal{U}_i^{NL}$ are the energy components associated with the linear and nonlinear strain terms, respectively. Here, E is the Young's modulus, and h is the structural thickness. The dependence of E to θ accounts for possible elastic anisotropy, which, most notably, is the case for (100) Si wafers.

Beams. Connecting beam#i and supporting beams#i are located at the angles $\theta_{c,i}=(i-1)\frac{\pi}{2n}$ and $\theta_{s,i}=(2i-1)\frac{\pi}{4n}$, respectively, where $i=1:4n$. We denote by $\vartheta_{c,i}$ and $\vartheta_{s,i}$ the deflection curves of connecting beam#i and supporting beam#i, respectively. As the coordinates, we use the abscissa, x along the beam's centerline and the ordinate, y orthogonal to the centerline (see Fig. 4(b)). The connecting (supporting) beams all have a fixed length of $l_{c(s)}$, but we consider the variable width $w_{c(s),i}(x)$ for connecting (supporting) beam#i to account for imperfections, resulting in variable area, $A_{c(s),i}(x)$ and second moment of area, $I_{c(s),i}(x)$ of the beam's cross-section. The displacement field of connecting (supporting) beam#i is given by [28]

$$\begin{aligned} u_{x,i}^{c(s)}(x,y,t) &= -y\frac{\partial\vartheta_{c(s),i}}{\partial x}(x,t),\\ u_{y,i}^{c(s)}(x,y,t) &= \vartheta_{c(s),i}(x,t),\end{aligned} \tag{7}$$

and the resulting strain is

$$\varepsilon_{xx,i}^{c(s)} = -y\frac{\partial^2\vartheta_{c(s),i}}{\partial x^2}(x,t). \tag{8}$$

We obtain the connecting (supporting) beam#i's strain energy as

$$\mathcal{U}_{c(s),i}^L = \frac{1}{2}hE(\theta_{c(s),i})\int_0^{l_{c(s)}}\int_{-\frac{w_{c(s),i}(x)}{2}}^{\frac{w_{c(s),i}(x)}{2}}\varepsilon_{xx,i}^{c(s)\,2}(x,y,t)\mathrm{d}y\mathrm{d}x. \tag{9}$$

Based on Eqs. (6) and (9), we can decompose the total strain energy into linear and nonlinear parts:

$$\begin{aligned}\mathcal{U} &= \mathcal{U}^L + \mathcal{U}^{NL},\\ \mathcal{U}^L &= \mathcal{U}_1^L + \mathcal{U}_2^L + \sum_{i=1}^{4n}\mathcal{U}_{c,i}^L + \mathcal{U}_{s,i}^L,\\ \mathcal{U}^{NL} &= \mathcal{U}_2^{NL}.\end{aligned} \tag{10}$$

2.3. Boundary conditions

The displacement fields are subject to the following kinematic constraints that arise from ring-beam connections:

1. *Connecting beam#i:* we have

$$\bar{u}_{r,1}\left(-\frac{w_1}{2},\theta_{c,i},t\right)=\bar{u}_{r,2}\left(\frac{w_2}{2},\theta_{c,i},t\right),\ i=1:4n, \tag{11}$$

which states that the rings both have the same radial displacement at $\theta=\theta_{c,i}$ (Fig. 5(a)). Furthermore, the following deflection/slope continuity conditions hold (Fig. 5(b)):

$$\begin{aligned}&\vartheta_{c,i}(0,t)=\bar{u}_{\theta,2}\left(\frac{w_2}{2},\theta_{c,i},t\right),\\ &\frac{\partial\vartheta_{c,i}}{\partial x}(0,t)=\gamma_2(\theta_{c,i},t),\\ &\vartheta_{c,i}(l_c,t)=\bar{u}_{\theta,1}\left(-\frac{w_1}{2},\theta_{c,i},t\right),\\ &\frac{\partial\vartheta_{c,i}}{\partial x}(l_c,t)=\gamma_1(\theta_{c,i},t),\ i=1:4n.\end{aligned} \tag{12}$$

2. *Supporting beam#i:* we have

$$\bar{u}_{r,2}\left(-\tfrac{w_2}{2},\theta_{s,i},t\right)=\Delta_i(t),\ \ i=1:4n. \tag{13}$$

Here, $\Delta_i(.)$ is the stress-induced displacement that the supporting beam transmits to Ring#2 (Fig. 5(c)). We also have the following deflection/slope continuity conditions (Fig. 5(d)):

$$\begin{aligned}&\vartheta_{s,i}(0,t)=0,\\&\frac{\partial\vartheta_{s,i}}{\partial x}(0,t)=0,\\&\vartheta_{s,i}(l_s,t)=\bar{u}_{\theta,2}\left(-\tfrac{w_2}{2},\theta_{s,i},t\right),\\&\frac{\partial\vartheta_{s,i}}{\partial x}(l_s,t)=\gamma_2(\theta_{s,i},t),\ \ i=1:4n.\end{aligned} \tag{14}$$

2.4. Mode shapes

The inextensible vibration of Ring#1 corresponds to a displacement field of the form

$$\begin{aligned}u_{\theta,1}(\theta,t)&=-f_{1,1}(\theta)Q_1(t)-f_{2,1}(\theta)Q_2(t),\\u_{r,1}(\theta,t)&=f'_{1,1}(\theta)Q_1(t)+f'_{2,1}(\theta)Q_2(t),\end{aligned} \tag{15}$$

where

$$f_{1,1}(\theta)=\frac{\sin(n\theta)}{n},\ \ f_{2,1}(\theta)=-\frac{\cos(n\theta)}{n}, \tag{16}$$

are the $n\theta$-mode shapes and Q_1, Q_2 are the generalized coordinates. Taking the extensibility of the Ring#2's centerline into account, we parametrize its displacement field as

$$\begin{aligned}u_{\theta,2}(\theta,t)&=-\mathcal{W}_\theta(\theta,t)-f_{1,2}(\theta)Q_1(t)-f_{2,2}(\theta)Q_2(t),\\u_{r,2}(\theta,t)&=\mathcal{W}_r(\theta,t)+f'_{1,2}(\theta)Q_1(t)+f'_{2,2}(\theta)Q_2(t),\end{aligned} \tag{17}$$

where $f_{1,2}(\theta)$ and $f_{2,2}(\theta)$ are the two orthogonal mode shapes of Ring#2 corresponding to the generalized coordinates Q_1 and Q_2, respectively. The functions $\mathcal{W}_r(\theta,t)$ and $\mathcal{W}_\theta(\theta,t)$ are bias-like terms that account for the nonhomogeneous boundary conditions caused by the displacements $\Delta_i(t)$. For the beams, we have

$$\begin{aligned}\vartheta_{c,i}(x,t)&={}_1\varpi_{c,i}(x)Q_1(t)+{}_2\varpi_{c,i}(x)Q_2(t),\\\vartheta_{s,i}(x,t)&={}_1\varpi_{s,i}(x)Q_1(t)+{}_2\varpi_{s,i}(x)Q_2(t),\end{aligned} \tag{18}$$

where ${}_1\varpi_{c(s),i}(x)$ and ${}_2\varpi_{c(s),i}(x)$, $i=1:4n$, are the beam mode shapes corresponding to Q_1 and Q_2, respectively. According to Eqs. (17) and (18), a complete description of the gyroscope's displacement fields amounts to calculation of the unknown mode shapes $\mathcal{W}_\theta, \mathcal{W}_r, f_{1,2}, f_{2,2}$, ${}_1\varpi_{c(s),i}$ and ${}_2\varpi_{c(s),i}$ subject to the boundary conditions (11)–(14). A calculation procedure for $f_{1,2}$, $f_{2,2}$, ${}_1\varpi_{c(s),i}$, and ${}_2\varpi_{c(s),i}$ is elaborated in [20]; hence, we turn our focus on $\mathcal{W}_r$ and $\mathcal{W}_\theta$. According to Eqs. (13) and (14), $\mathcal{W}_r(\theta,t)$ and $\mathcal{W}_\theta(\theta,t)$ satisfy the following boundary conditions:

1. *Connecting beam#i:* no radial displacement and no cross-sectional rotation:

$$\begin{aligned}&\mathcal{W}_r(\theta_{c,i},t)=0,\ \ \frac{\partial\mathcal{W}_r}{\partial\theta}(\theta_{c,i},t)=0,\\&\mathcal{W}_\theta(\theta_{c,i},t)=0,\ \ i=1:4n.\end{aligned} \tag{19}$$

2. *Supporting beam#i:* stress-induced radial displacement and no cross-sectional rotation:

$$\begin{aligned}&\mathcal{W}_r(\theta_{s,i},t)=\Delta_i(t),\ \ \frac{\partial\mathcal{W}_r}{\partial\theta}(\theta_{s,i},t)=0,\\&\mathcal{W}_\theta(\theta_{s,i},t)=0,\ \ i=1:4n.\end{aligned} \tag{20}$$

Mathematically, any pair of functions $(\mathcal{W}_\theta,\mathcal{W}_r)$ that satisfy (19) and (20) constitutes an admissible choice to be used in Eq. (17). We, however, impose additional conditions to ensure that the calculated functions do not deviate drastically from the true, physical displacement field. For this purpose, at any given time instant $t\geq 0$, we require $\mathcal{W}_r(\theta,t)$ and $\mathcal{W}_\theta(\theta,t)$ to be the radial and tangential components,

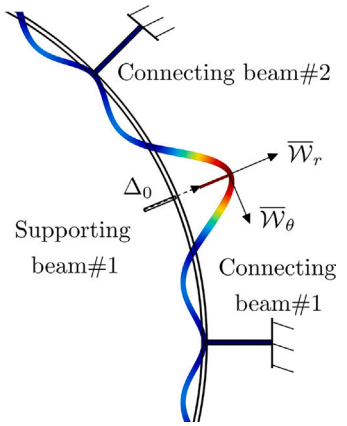

Fig. 6. Displacement field of Ring#2 generated by the radial displacement at supporting beam#1.

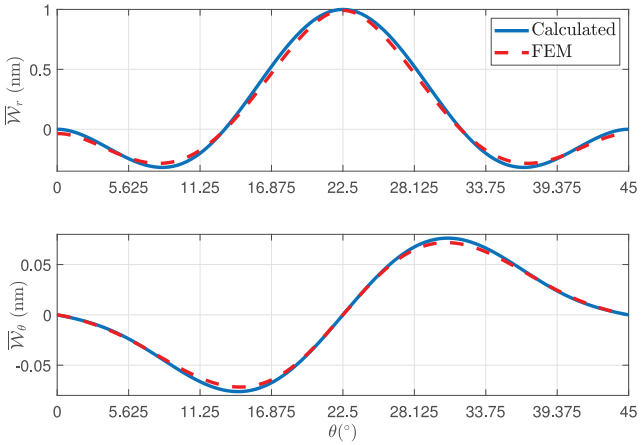

Fig. 7. Displacement field $\left(\overline{\mathcal{W}}_r,\overline{\mathcal{W}}_\theta\right)$ of Ring#2 under the imposed displacement $\Delta_0=1$ nm by supporting beam#1 at 22.5°; calculated versus FEM.

respectively, of the equilibrium displacement field that the applied displacements $\Delta_i(t)$, $i=1:4n$, generate in Ring#2. Taking advantage of the symmetry of the beams' arrangement, we calculate $\mathcal{W}_r$ and $\mathcal{W}_\theta$ by the following steps:

1. Consider the portion $\theta\in[0,\frac{\pi}{2n}]$ of Ring#2, which contains connecting beams#1, 2 and supporting beam#1; assume a given radial displacement Δ_0 that supporting beam#1 exerts on Ring#2.
2. Calculate the functions $\overline{\mathcal{W}}_r(\theta)$ and $\overline{\mathcal{W}}_\theta(\theta)$ for $\theta\in[0,\frac{\pi}{2n}]$ that correspond to the static equilibrium displacement field in step 1; this displacement field is illustrated in Fig. 6.
3. For any portion $\theta\in[\frac{\pi}{2n}(i-1),\frac{\pi}{2n}i]$, $i=1:4n$, of Ring#2 with the given displacement $\Delta_i(t)$, we have

$$\begin{aligned}\mathcal{W}_\theta(\theta,t)&=\frac{\Delta_i(t)}{\Delta_0}\overline{\mathcal{W}}_\theta\left(\theta-\tfrac{\pi}{2n}(i-1)\right),\\\mathcal{W}_r(\theta,t)&=\frac{\Delta_i(t)}{\Delta_0}\overline{\mathcal{W}}_r\left(\theta-\tfrac{\pi}{2n}(i-1)\right).\end{aligned} \tag{21}$$

Calculating $\overline{\mathcal{W}}_r$ and $\overline{\mathcal{W}}_\theta$. The extensional strain and cross-sectional rotation angle corresponding to the displacement field $(\overline{\mathcal{W}}_r,\overline{\mathcal{W}}_\theta)$ are given by

$$\begin{aligned}\bar{\varepsilon}_{0,2}(\theta)&=\frac{1}{R_2}\left(\overline{\mathcal{W}}_r(\theta)-\overline{\mathcal{W}}'_\theta(\theta)\right),\\\bar{\gamma}_{0,2}(\theta)&=\frac{-1}{R_2}\left(\overline{\mathcal{W}}_\theta(\theta)+\overline{\mathcal{W}}'_r(\theta)\right),\end{aligned} \tag{22}$$

Box 1: Quadratic programming for calculating $\overline{\mathcal{W}}_r(\theta) \approx \chi_r^\top(\theta)\alpha_r^*$ and $\overline{\mathcal{W}}_\theta(\theta) \approx \chi_\theta^\top(\theta)\alpha_\theta^*$

$$\begin{bmatrix}\alpha_\theta^* \\ \alpha_r^*\end{bmatrix} = \arg\min_{\alpha_\theta,\alpha_r\in\mathbb{R}^N} \frac{1}{2}\begin{bmatrix}\alpha_\theta \\ \alpha_r\end{bmatrix}^\top \begin{bmatrix}P_{\theta\theta} & P_{\theta r} \\ P_{\theta r}^\top & P_{rr}\end{bmatrix}\begin{bmatrix}\alpha_\theta \\ \alpha_r\end{bmatrix} \text{ subject to } \begin{cases} A_\theta\alpha_\theta = 0_{3\times1}, \\ A_r\alpha_r = \Delta_0 b_r, \end{cases} \quad \text{where}$$

$$P_{\theta\theta} = \left(\frac{EA_2}{R_2} + \frac{EI_2}{R_2^3}\right)\int_0^{\frac{\pi}{2n}} \chi_\theta'(\theta)\chi_\theta'^\top(\theta)\mathrm{d}\theta,\ P_{rr} = \frac{EA_2}{R_2}\int_0^{\frac{\pi}{2n}} \chi_r(\theta)\chi_r^\top(\theta)\mathrm{d}\theta + \frac{EI_2}{R_2^3}\int_0^{\frac{\pi}{2n}} \chi_r''(\theta)\chi_r''^\top(\theta)\mathrm{d}\theta,$$

$$P_{\theta r} = -\frac{EA_2}{R_2}\int_0^{\frac{\pi}{2n}} \chi_\theta'(\theta)\chi_r^\top(\theta)\mathrm{d}\theta + \frac{EI_2}{R_2^3}\int_0^{\frac{\pi}{2n}} \chi_\theta'(\theta)\chi_r''^\top(\theta)\mathrm{d}\theta,$$

$$A_\theta = \left[\chi_\theta(0), \chi_\theta\left(\tfrac{\pi}{4n}\right), \chi_\theta\left(\tfrac{\pi}{2n}\right)\right]^\top, A_r = \left[\chi_r(0), \chi_r'(0), \chi_r\left(\tfrac{\pi}{4n}\right), \chi_r'\left(\tfrac{\pi}{4n}\right), \chi_r\left(\tfrac{\pi}{2n}\right), \chi_r'\left(\tfrac{\pi}{2n}\right)\right]^\top,\ b_r = [0,0,1,0,0,0]^\top.$$

respectively. We now minimize the strain potential energy stored in Ring#2 over $\theta \in [0, \frac{\pi}{2n}]$,

$$\mathcal{U} = \frac{1}{2}EA_2R_2\int_0^{\frac{\pi}{2n}} \bar{\varepsilon}_{0,2}^2(\theta)\mathrm{d}\theta + \frac{EI_2}{2R_2}\int_0^{\frac{\pi}{2n}} \bar{\gamma}_{0,2}'^2(\theta)\mathrm{d}\theta, \tag{23}$$

considering the kinematic constraints that follow from (19) and (20):

$$\begin{aligned} &\overline{\mathcal{W}}_r(0) = 0, \overline{\mathcal{W}}_r'(0) = 0, \overline{\mathcal{W}}_\theta(0) = 0, \\ &\overline{\mathcal{W}}_r\left(\tfrac{\pi}{4n}\right) = \Delta_0, \overline{\mathcal{W}}_r'\left(\tfrac{\pi}{4n}\right) = 0, \overline{\mathcal{W}}_\theta\left(\tfrac{\pi}{4n}\right) = 0, \\ &\overline{\mathcal{W}}_r\left(\tfrac{\pi}{2n}\right) = 0, \overline{\mathcal{W}}_r'\left(\tfrac{\pi}{2n}\right) = 0, \overline{\mathcal{W}}_\theta\left(\tfrac{\pi}{2n}\right) = 0. \end{aligned} \tag{24}$$

The above formulation is a variational problem; following the Ritz method [28], we convert it into numerical optimization using the parametrizations

$$\begin{aligned} \overline{\mathcal{W}}_\theta(\theta) &\approx \chi_\theta^\top(\theta)\alpha_\theta, \\ \overline{\mathcal{W}}_r(\theta) &\approx \chi_r^\top(\theta)\alpha_r, \end{aligned} \tag{25}$$

where $\chi_\theta(.),\ \chi_r(.) \in \mathbb{R}^N$ (with $N \geq 1$) are the vectors of suitable basis functions, and $\alpha_\theta,\ \alpha_r \in \mathbb{R}^N$ are the corresponding coefficients. By substituting (25) into (23) and (24), we obtain a quadratic programming (QP) problem in the unknowns α_θ, α_r, which is given in Box 1.

Basis functions $\chi_r(\theta),\ \chi_\theta(\theta)$. Since $\overline{\mathcal{W}}_r$ has an even symmetry about $\theta = \frac{\pi}{4n}$ and $\overline{\mathcal{W}}_r - \overline{\mathcal{W}}_\theta' \approx 0$, we use the following polynomial basis functions:

$$\begin{aligned} \chi_r(\theta) &= \left[1, \left(\theta - \tfrac{\pi}{4n}\right)^2, \ldots, \left(\theta - \tfrac{\pi}{4n}\right)^{2N-2}\right]^\top, \\ \chi_\theta(\theta) &= \left[\left(\theta - \tfrac{\pi}{4n}\right), \ldots, \tfrac{1}{2N-1}\left(\theta - \tfrac{\pi}{4n}\right)^{2N-1}\right]^\top. \end{aligned} \tag{26}$$

For a unit displacement of $\Delta_0 = 1$ nm and $N = 6$ basis functions, Fig. 7 shows the comparative graphs of our calculated functions $\overline{\mathcal{W}}_r(\theta)$ and $\overline{\mathcal{W}}_\theta(\theta)$ and those obtained from FEM (done in COMSOL Multiphysics). Taking FEM results as the reference, the small RMS errors 3.5×10^{-2} nm and 2.6×10^{-3} nm of the calculated $\overline{\mathcal{W}}_r(\theta)$ and $\overline{\mathcal{W}}_\theta(\theta)$, respectively, confirm our method's accuracy.

2.5. Electrostatic softening

As shown in Fig. 8(a), we use 16 pairs of electrodes around Ring#1 for differential sensing, actuation, and control purposes. The i-th pair is centered at the angle $\theta_{e,i}$ with the outer and inner angular spans and gaps of $\Delta\theta_{1,i}$, $g_\mathcal{O}(\theta,t)$ and $\Delta\theta_{2,i}$, $g_\mathcal{I}(\theta,t)$, respectively (see Fig. 8(b)). The (θ,t)-dependence of $g_\mathcal{I}, g_\mathcal{O}$ accounts for stress-induced gap variations. The total electrostatic potential energy is

$$\mathcal{U}_e = \sum_{i=1}^{16} \frac{1}{2}C_{1,i}V_{1,i}^2 + \frac{1}{2}C_{2,i}V_{2,i}^2, \tag{27}$$

where $C_{1,i}, V_{1,i}$ and $C_{2,i}, V_{2,i}$ are the capacitances and voltage differences between Ring#1 and the outer and inner electrodes, respectively [6].

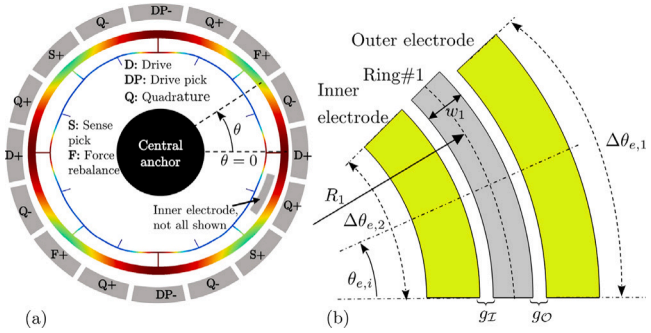

Fig. 8. Configuration of electrodes (a) and modeling schematics for a pair of electrodes (b).

2.6. Stiffness matrix

The total stiffness matrix $K \in \mathbb{R}^{2\times2}$ is given by

$$K = K_m + K_s - K_e, \tag{28}$$

where

- $K_m = [k_{ij}^m] \in \mathbb{R}^{2\times2}$ is the nominal mechanical stiffness matrix that one would observe in the absence of external stress effects, and it follows from the linear strains:
$$k_{ij}^m = \frac{\partial^2\mathcal{U}^L}{\partial Q_i \partial Q_j}\Big|_{Q_1,Q_2=0}. \tag{29}$$
- $K_s = [k_{ij}^s] \in \mathbb{R}^{2\times2}$ is the *stress stiffness* matrix; the stress-induced displacements Δ_i alter the strain energy stored in Ring#2, and the subsequent effect on the stiffness is associated with the geometric nonlinearity, i.e., the nonlinear strain terms:
$$k_{ij}^s = \frac{\partial^2\mathcal{U}^{NL}}{\partial Q_i \partial Q_j}\Big|_{Q_1,Q_2=0}. \tag{30}$$
- $K_e = [k_{ij}^e] \in \mathbb{R}^{2\times2}$ is the electrostatic softening matrix:
$$k_{ij}^e = \frac{\partial^2\mathcal{U}_e}{\partial Q_i \partial Q_j}\Big|_{Q_1,Q_2=0}. \tag{31}$$

The detailed expanded expressions for (29)–(31) are provided in Box 2.

2.7. Further remarks on stress stiffness

Remark 1. Neglecting second-order and product strain terms, we obtain the linearized expression $k_{ij}^s \approx k_{ij}^{\text{ext}} + k_{ij}^{\text{ben}}$ for the stress stiffness

Box 2: Formulas for nominal, stress, and electrostatic stiffness matrices

- **Nominal stiffness matrix:** $k^m_{ij} = k_{ij,1} + k_{ij,2} + k_{ij,c} + k_{ij,s}$;
  - Ring#ℓ, $\ell = 1, 2$:
  - Connecting (supporting) beams:

$$k_{ij,\ell} = \frac{1}{R_\ell^3}\int_0^{2\pi} F'_{i,\ell}(\theta)F'_{j,\ell}(\theta)E(\theta)I_\ell(\theta)\mathrm{d}\theta, \qquad k_{ij,c(s)} = \sum_{\ell=1}^{4n} E(\theta_{c(s),\ell})\int_0^{l_{c(s)}} {}_i\varpi''_{c(s),\ell}(x)\,{}_j\varpi''_{c(s),\ell}(x)I_{c(s),\ell}(x)\mathrm{d}x,$$

  where $F_{i,\ell}(\theta) := f_{i,\ell}(\theta) + f''_{i,\ell}(\theta)$, $I_\ell(\theta) = \frac{1}{12}hw_\ell^3(\theta)$ for $\ell = 1, 2$, and $I_{c(s),\ell}(x) = \frac{1}{12}hw^3_{c(s),\ell}(x)$ for $\ell = 1 : 4n$.
- **Stress stiffness matrix:** $k^s_{ij}(t) \approx k^{\text{ext}}_{ij}(t) + k^{\text{ben}}_{ij}(t)$;

$$k^{\text{ext}}_{ij}(t) = \frac{1}{R_2}\int_0^{2\pi} E(\theta)A_2(\theta)\varepsilon_{0,2}(\theta,t)F_{i,2}(\theta)F_{j,2}(\theta)\mathrm{d}\theta,$$

$$k^{\text{ben}}_{ij}(t) = \frac{1}{R_2^3}\int_0^{2\pi} E(\theta)I_2(\theta)\varepsilon_{0,2}(\theta,t)\left\{F_{i,2}(\theta)F_{j,2}(\theta) + 3F'_{i,2}(\theta)F'_{j,2}(\theta)\right\}\mathrm{d}\theta$$
$$+ \frac{2}{R_2^3}\int_0^{2\pi} E(\theta)I_2(\theta)\frac{\partial}{\partial\theta}\{\gamma_{0,2}(\theta,t)F_{i,2}(\theta)F_{j,2}(\theta)\}\mathrm{d}\theta.$$

  where $A_2(\theta) = hw_2(\theta)$, $\varepsilon_{0,2}(\theta,t) = \frac{1}{R_2}\left(\mathcal{W}_r(\theta,t) - \frac{\partial}{\partial\theta}\mathcal{W}_\theta(\theta,t)\right)$, and $\gamma_{0,2}(\theta,t) = \frac{-1}{R_2}\left(\mathcal{W}_\theta(\theta,t) + \frac{\partial}{\partial\theta}\mathcal{W}_r(\theta,t)\right)$.
  - *Online calculation:* $k^s_{ij}(t) \approx \sum_{\ell=1}^{4n}\frac{\Delta_\ell(t)}{\Delta_0}\overline{k}_{ij,\ell}$;

$$\overline{k}_{ij,\ell} = \frac{1}{R_2}\int_{\frac{\pi(\ell-1)}{2n}}^{\frac{\pi\ell}{2n}} E(\theta)A_2(\theta)\overline{\varepsilon}_{0,2}(\theta - \tfrac{\pi(\ell-1)}{2n})F_{i,2}(\theta)F_{j,2}(\theta)\mathrm{d}\theta$$
$$+ \frac{1}{R_2^3}\int_{\frac{\pi(\ell-1)}{2n}}^{\frac{\pi\ell}{2n}} E(\theta)I_2(\theta)\overline{\varepsilon}_{0,2}(\theta - \tfrac{\pi(\ell-1)}{2n})\{F_{i,2}(\theta)F_{j,2}(\theta)$$
$$+ 3F'_{i,2}(\theta)F'_{j,2}(\theta)\}\mathrm{d}\theta + \frac{2}{R_2^3}\int_{\frac{\pi(\ell-1)}{2n}}^{\frac{\pi\ell}{2n}} E(\theta)I_2(\theta)\frac{\mathrm{d}}{\mathrm{d}\theta}\{\overline{\gamma}_{0,2}(\theta - \tfrac{\pi(\ell-1)}{2n})F_{i,2}(\theta)F_{j,2}(\theta)\}\mathrm{d}\theta.$$

- **Electrostatic softening:** $\epsilon_0 = 8.8542\times10^{-12}$ F/m is the vacuum permittivity;

$$k^e_{ij}(t) = \epsilon_0 h\sum_{\ell=1}^{16} V^2_{1,\ell}\int_{\theta_{e,\ell}-\frac{\Delta\theta_{1,\ell}}{2}}^{\theta_{e,\ell}+\frac{\Delta\theta_{1,\ell}}{2}} \frac{R_1 + \frac{w(\theta)}{2}}{g^3_{\mathcal{O}}(\theta,t)}f'_{i,1}(\theta)f'_{j,1}(\theta)\mathrm{d}\theta$$
$$+ V^2_{2,\ell}\int_{\theta_{e,\ell}-\frac{\Delta\theta_{2,\ell}}{2}}^{\theta_{e,\ell}+\frac{\Delta\theta_{2,\ell}}{2}} \frac{R_1 - \frac{w(\theta)}{2}}{g^3_{\mathcal{I}}(\theta,t)}f'_{i,1}(\theta)f'_{j,1}(\theta)\mathrm{d}\theta.$$

in Box 2. The first term denotes an extensional stiffness, $k^{\text{ext}}_{ij} \propto EA_2/R_2$ while the second one stands for bending stiffness, $k^{\text{ben}}_{ij} \propto EI_2/R_2^3$. Since $k^{\text{ben}}_{ij}/k^{\text{ext}}_{ij} \propto (w_2/R_2)^2$, for a narrow ring, the extensional part has a much larger contribution to the stress stiffness than the bending part. It is worth mentioning that the extensional stiffness k^{ext}_{ij} does not appear in the k^s_{ij} formula if one proceeds with the inextensibility assumption prevalent in the literature.

Remark 2. The stress stiffness varies with time as it depends on the displacements $\Delta_i(t)$. Based on the procedure detailed in Section 2.4 and Eq. (21), we simplify the online calculation of $k^s_{ij}(t)$ as

$$k^s_{ij}(t) \approx \sum_{\ell=1}^{4n}\frac{\Delta_\ell(t)}{\Delta_0}\overline{k}_{ij,\ell}, \tag{32}$$

where $\overline{k}_{ij,\ell}$ are given in Box 2. The interpretation of Eq. (32) is as follows. We first calculate the displacement field $(\overline{\mathcal{W}}_r(\theta), \overline{\mathcal{W}}_\theta(\theta))$ resulting from a unit displacement Δ_0 at supporting beam#1. This calculated displacement field then enables us to compute $\overline{k}_{ij,\ell}$, the unit stiffness matrix across the portion $\theta \in [\frac{\pi}{2n}(\ell-1), \frac{\pi}{2n}\ell]$, $\ell = 1 : 4n$, of Ring#2. At any given time t with the displacements $\Delta_\ell(t)$ at the supporting beams, we obtain the stress stiffness $k^s_{ij}(t)$ as a linear combination of the unit stiffness matrices with the weights $\Delta_\ell(t)/\Delta_0$. In the absence of imperfections and elastic anisotropy, the calculation of stress stiffness is further simplified.

Remark 3. The displacement field $\left(\overline{\mathcal{W}}_r, \overline{\mathcal{W}}_\theta\right)$ in Fig. 6 is symmetric with respect to both $n\theta$-mode shapes of the inner ring, and, as a result, $k^s_{11} = k^s_{22}$. However, this displacement field spoils the orthogonality of the $n\theta$-mode shapes, resulting in a stress-induced stiffness coupling. For example, with our VRG's parameters, we have $k^s_{12}/k^s_{11} \approx 1.8\%$ under $\Delta_0 = 1$ nm displacement.

2.8. Mass matrix

Detailed derivations of the mass matrix $M = [m_{ij}] \in \mathbb{R}^{2\times2}$ and Coriolis mass m_C (i.e., the effective mass that participates in the Coriolis effect) can be found in [20].

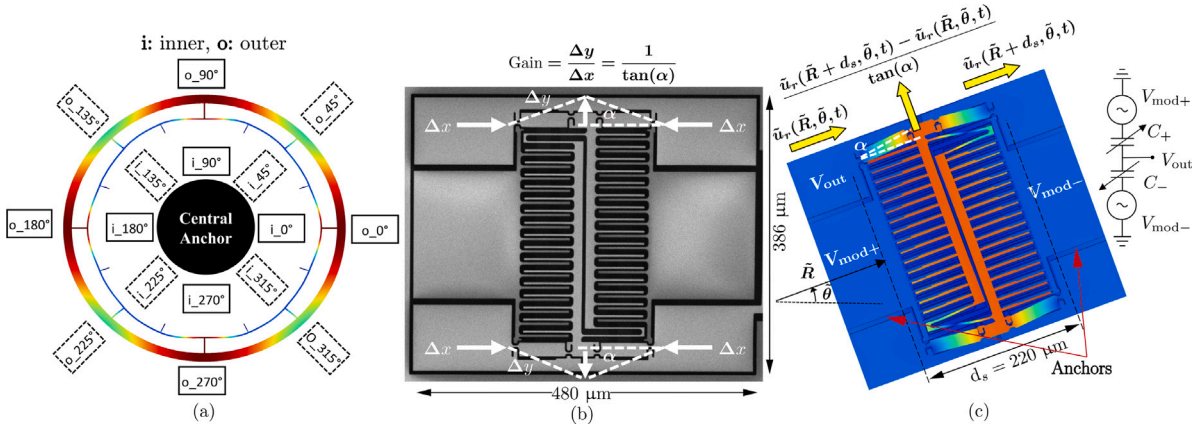

Fig. 9. Stress sensors' arrangement (a), SEM (b), and working principle (c).

3. Stress sensors

As shown in Fig. 9(a), we have distributed 16 stress sensors with 45° symmetry across the gyroscope, eight in the internal structure and eight outside Ring#1. Fig. 9(c) explains the working principle of the stress sensors as capacitive strain gauges that measure the local displacement gradient of the substrate via their anchors [5,29]. Following the notation in the figure, consider a stress sensor located at the radial position $\tilde{R}$ and the polar angle $\tilde{\theta}$. Let $\tilde{u}_r(r,\theta,t)$ be the radial component of the substrate's displacement field, and $\tilde{\varepsilon}_{rr}(r,\theta,t) = \partial\tilde{u}_r(r,\theta,t)/\partial r$ be the corresponding radial strain. Since

$$\tilde{u}_r(\tilde{R}+d_s,\tilde{\theta},t) - \tilde{u}_r(\tilde{R},\tilde{\theta},t) \approx \tilde{\varepsilon}_{rr}(\tilde{R},\tilde{\theta},t)d_s, \tag{33}$$

the stress sensor's output is proportional to the local radial strain, and, in turn, to the radial stress, $\tilde{\sigma}_{rr} = E\tilde{\varepsilon}_{rr}$. On this basis, we use the stress sensors outputs to interpolate the radial strain field across the substrate. The interpolation amounts to setting forth an approximation of the form

$$\tilde{\varepsilon}_{rr}(r,\theta,t) \approx \sum_{i=1}^{\tilde{N}} \phi_i(r,\theta)\alpha_i(t) = \phi^{\top}(r,\theta)\alpha(t), \tag{34}$$

where $\phi(r,\theta) := [\phi_1(r,\theta),\dots,\phi_{\tilde{N}}(r,\theta)] \in \mathbb{R}^{\tilde{N}}$ is a vector of suitable basis functions, $\alpha(t) = [\alpha_1(t),\dots,\alpha_{\tilde{N}}]^{\top} \in \mathbb{R}^{\tilde{N}}$ is the vector of basis functions' coefficients, and $\tilde{N} \geq 1$ is the number of basis functions. At time t, we obtain the optimal vector of coefficients, $\alpha^*(t)$ by solving the following least-squares problem:

$$\alpha^*(t) := \arg\min_{\alpha\in\mathbb{R}^{\tilde{N}}} \frac{1}{2}\sum_{i,j}\left(\tilde{\varepsilon}_{ij}(t) - \phi^{\top}(\tilde{R}_i,\tilde{\theta}_j)\alpha\right)^2, \tag{35}$$

where $\tilde{\varepsilon}_{ij}$ is the output of the stress sensor located at $(\tilde{R}_i,\tilde{\theta}_j)$. We then obtain the substrate's radial displacement field as

$$\tilde{u}_r(r,\theta,t) \approx \int_0^r \phi^{\top}(\varrho,\theta)\alpha^*(t)\mathrm{d}\varrho, \tag{36}$$

which provides us with the displacements $\Delta_i(t)$ at the supporting beams and the electrostatic gaps $g_{\mathcal{I}}(\theta,t)$, $g_{\mathcal{O}}(\theta,t)$ that are required for calculating the stress stiffness and softening matrices, respectively. The main steps of this procedure are explained by the flowchart in Fig. 10.

Basis functions $\phi(r,\theta)$. The strain field $\tilde{\varepsilon}_{rr}(r,\theta,t)$ is continuous, 2π-periodic in θ, and, therefore, admits a convergent Fourier series. Hence, assuming a linear variation in the r-direction, we use the following basis functions for $\ell = 1,2,\dots$:

$$1, r, \cos(\ell\theta), r\cos(\ell\theta), \sin(\ell\theta), r\sin(\ell\theta). \tag{37}$$

3.1. Comments on accuracy and performance of stress sensors

Accuracy. Ideally, the stress sensors do not respond to the tangential strain up to the first order [29]. Tangential strains rotate the entire sensor, resulting in a negligible response due to the differential sensing mechanism. However, considering fabrication tolerances, tangential strains could affect practical sensors and contaminate the radial strain measurements.

Performance. The stress sensors exhibit a mechanical resonance frequency of around 300 kHz, while they operate at 10 kHz. Hence, electronics noise dominates the performance of the stress sensors. We calculated the resolution of the stress sensor as 0.9 kPa/$\sqrt{\text{Hz}}$, corresponding to 5.3 nano-Strain. Given the substantial levels of stress that we apply during the tests, this resolution proves adequate for our analysis. In practical stress calibration scenarios, we can take advantage of the slow variations of stress and further improve the resolution by heavily averaging the stress sensor outputs.

4. Analysis of stress effects

The eigenvalue problem

$$Kv = \omega^2 Mv \tag{38}$$

provides us with the following key vibrational properties [20]: (1) the two natural frequencies ω_1,ω_2 as the eigenvalues; (2) the orientation of mode shapes defined by the eigenvectors $v_1,v_2 \in \mathbb{R}^2$. In an ideal VRG, the two $n\theta$-mode shapes share the same effective mass and stiffness. In turn, the mode shapes have a matched frequency ($\omega_1 = \omega_2$) and are in alignment with the designated drive $\theta = 0$ and sense $\theta = \frac{\pi}{2n}$ axes. Fabrication-induced nonuniformities alter the ideal mass and stiffness distribution across the mechanical structure, and environmental variations such as stress and temperature perturb the stiffness. These factors manifest in the M and K matrices as mismatches between the diagonal entries and nonzero off-diagonal coupling terms. Therefore, in a nonideal VRG, we could have a frequency split between the mode shapes, and their orientation could deviate from the nominal drive and sense axes. Fig. 11 illustrates the modal space of the nonideal VRG with the rotated mode shapes $\cos(n\theta-\psi_1)$ and $\sin(n\theta-\psi_1)$, where ψ_1 and ψ_2 are the angles between the eigenvectors v_1 and v_2 and Q_1- and Q_2-axes, respectively. The eigenvectors define a principal coordinate system $\{Q_1^*,Q_2^*\}$ in which the mass and stiffness matrices assume the diagonal forms

$$M^* = T^{\top}MT = \begin{bmatrix} m_1^* & 0 \\ 0 & m_2^* \end{bmatrix},$$
$$K^* = T^{\top}KT = \begin{bmatrix} m_1^*\omega_1^2 & 0 \\ 0 & m_2^*\omega_2^2 \end{bmatrix}, \tag{39}$$

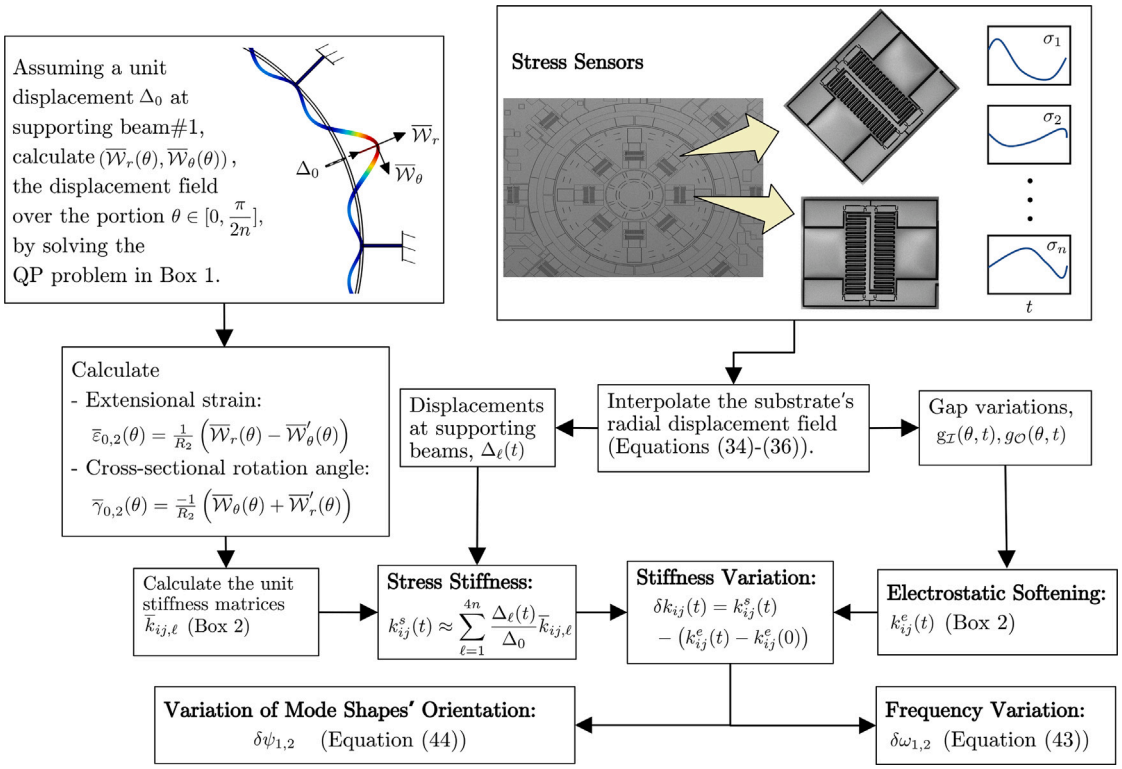

Fig. 10. Flowchart of calculating stress stiffness, electrostatic softening, and their effects on vibrational properties using the stress sensors' outputs.

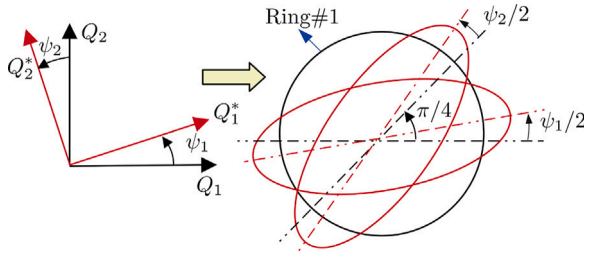

Fig. 11. Principal coordinate system and rotated mode shapes.

where

$$T = \begin{bmatrix} \cos(\psi_1) & -\sin(\psi_2) \\ \sin(\psi_1) & \cos(\psi_2) \end{bmatrix} \tag{40}$$

is the transformation matrix from $\{Q_1^*, Q_2^*\}$ coordinates to $\{Q_1, Q_2\}$ [20]. We consider the damping matrix in the principal coordinate system as

$$D^* = \begin{bmatrix} m_1^* \frac{\omega_1}{q_{f_1}} & d_{12}^* \\ d_{12}^* & m_2^* \frac{\omega_2}{q_{f_2}} \end{bmatrix} \tag{41}$$

where q_{f_1} and q_{f_2} are the quality factors of $\cos(n\theta - \psi_1)$ and $\sin(n\theta - \psi_1)$ modes, respectively, and d_{12}^* is the coefficient of damping coupling between the two modes.

4.1. Variations of vibrational properties

In the absence of stress, the total stiffness matrix is

$$K_0 = K_m - K_{e,0}, \tag{42}$$

where $K_{e,0} \in \mathbb{R}^{2\times 2}$ is the initial electrostatic stiffness matrix. The pair (M, K_0) is characterized by the frequencies $\omega_{1,0}, \omega_{2,0}$ and mode shape rotation angles $\psi_{1,0}, \psi_{2,0}$. In the presence of stress, the stiffness variation $\delta K = K_s - (K_e - K_{e,0})$ acts as a small perturbation of the initial stiffness matrix, i.e., $K_0 \mapsto K_0 + \delta K$. We can therefore perform an eigenvalue perturbation analysis [30] to approximate the variations of the vibrational properties:

1. **Eigenvalue variations, $\boldsymbol{\omega_{i,0} \mapsto \omega_{i,0} + \delta\omega_i}$:**

$$\delta\omega_i \approx \frac{\delta k_{ii}^*}{2m_i^*\omega_{i,0}},\ i = 1, 2; \tag{43}$$

we note that the initial frequency split between the modes, $\Delta\omega_0 := \omega_{1,0} - \omega_{2,0}$ is perturbed as well:

$$\begin{aligned} \Delta\omega_0 &\mapsto \Delta\omega_0 + \delta\omega_1 - \delta\omega_2, \\ \frac{\delta\omega_1 - \delta\omega_2}{\omega_{1,0}} &\approx \frac{\delta k_{11}^* - \delta k_{22}^*}{2m_1^*\omega_{1,0}^2} \\ &= \frac{\delta k_{11} - \delta k_{22}}{4k_{11}^*}\left(\cos(2\psi_{1,0}) + \cos(2\psi_{2,0})\right) \\ &+ \frac{\delta k_{12}}{2k_{11}^*}\left(\sin(2\psi_{1,0}) + \sin(2\psi_{2,0})\right), \end{aligned} \tag{44}$$

where $k_{11}^* = m_1^*\omega_{1,0}^2$.

2. **Eigenvector variations, $\boldsymbol{\psi_{i,0} \mapsto \psi_{i,0} + \delta\psi_i}$:**

$$\delta\psi_i \approx \frac{\delta k_{12}^*}{m_i^*(\omega_{1,0}^2 - \omega_{2,0}^2)},\ i = 1, 2. \tag{45}$$

In Eqs. (43) and (45), δk_{ij}^* are the components of δK in the principal coordinate system:

$$\delta k_{11}^* = \left(\frac{\delta k_{11} + \delta k_{22}}{2}\right) + \left(\frac{\delta k_{11} - \delta k_{22}}{2}\right)\cos(2\psi_{1,0})$$

$$+\delta k_{12}\sin(2\psi_{1,0}),$$
$$\delta k_{22}^{*}=\left(\frac{\delta k_{11}+\delta k_{22}}{2}\right)-\left(\frac{\delta k_{11}-\delta k_{22}}{2}\right)\cos(2\psi_{2,0})$$
$$-\delta k_{12}\sin(2\psi_{2,0}),$$
$$\delta k_{12}^{*}=\left(\frac{\delta k_{11}+\delta k_{22}}{2}\right)\sin(\psi_{1,0}-\psi_{2,0})-\left(\frac{\delta k_{11}-\delta k_{22}}{2}\right)$$
$$\times\sin(\psi_{1,0}+\psi_{2,0})+\delta k_{12}\cos(\psi_{1,0}+\psi_{2,0}). \tag{46}$$

4.2. Quadrature and in-phase errors

We define the force–displacement transfer functions $H_1(s)$ and $H_2(s)$ for the $\cos(n\theta-\psi_1)$ and $\sin(n\theta-\psi_1)$ modes, respectively, as

$$H_i(s)=\frac{1}{m_i^{*}}\frac{1}{s^2+BW_i s+\omega_i^2}, \tag{47}$$

where $BW_i=\omega_i/q_{f_i}$, $i=1,2$, are the bandwidths and s denotes the Laplace variable. In our VRG, a phase-locked loop (PLL) uses the outputs of the drive pick electrodes located at 90° and 270° as the feedback variables and generates an AC force of the form $\mathcal{F}(t)=\mathcal{F}_0\cos(\omega_1 t)$ along the $\theta=0$ axis via the drive electrodes at 0° and 180°. The sense electrodes located at 135° and 315° pick up the response $Q_2(t)$ along the $\theta=135°$ axis which then is demodulated (see Fig. 8 for the locations of electrodes). The rotation angles ψ_1 and ψ_2 of the mode shapes disturb this drive-sensing apparatus. The driving force actuates both modes, and the picked up signal $Q_2(t)$ is a mixture of the responses of both modes. Under the drive signal $\mathcal{F}(t)=\mathcal{F}_0\cos(\omega_1 t)$, the transfer functions (47) reduce to

$$H_1(\jmath\omega_1)=\frac{1}{m_1^{*}\omega_1 BW_1}\measuredangle-90°,$$
$$H_2(\jmath\omega_1)\approx\frac{1}{2m_2^{*}\omega_1|\Delta\omega|\sqrt{1+\left(\frac{BW_2}{2\Delta\omega}\right)^2}}\measuredangle-\beta_2, \tag{48}$$

where $\jmath$ denotes the imaginary unit, $\Delta\omega=\omega_1-\omega_2$, and β_2 is the phase of $H_2(\jmath\omega_1)$. A perturbation analysis-based procedure was used in [20] to derive the nonideal transfer function from the nominal drive at $\theta=0°$ to the nominal sense at $\theta=135°$, which gives us the response

$$Q_2(t)\approx\mathcal{A}\mathcal{F}_0\cos(\omega_1 t-\varphi)+\mathcal{B}\mathcal{F}_0\sin(\omega_1 t-\varphi), \tag{49}$$

where φ is the demodulation angle and

$$\mathcal{A}=A\sin(\varphi)-(B-SF^{-1}(\Omega_z+\Omega_{z,d}))\cos(\beta_2-\varphi),$$
$$\mathcal{B}=A\cos(\varphi)-(B-SF^{-1}(\Omega_z+\Omega_{z,d}))\sin(\beta_2-\varphi),$$
$$A=\frac{1}{2}\left|H_1(\jmath\omega_1)\right|\sin(2\psi_1),$$
$$B=\frac{1}{2}\left|H_2(\jmath\omega_1)\right|\sin(2\psi_2), \tag{50}$$
$$SF=\frac{-1}{2m_c\omega_1\left|H_1(\jmath\omega_1)\right|\left|H_2(\jmath\omega_1)\right|\cos^2(\psi_1-\psi_2)},$$
$$\Omega_{z,d}=\frac{d_{12}^{*}\cos(\psi_1+\psi_2)}{2m_c\cos^2(\psi_1-\psi_2)}.$$

We note that SF is the mechanical scale factor, and $\Omega_{z,d}$ is the equivalent rotation rate of the damping coupling. The demodulation angle φ is selected to compensate for the nonideal phase of the sense mode caused by electronics. Based on (49), we analyze the gyroscope's errors in two operation scenarios: mode-matched and mode-mismatched.

- *Mode-matched:* $\Delta\omega\approx0$ and $\beta_2-\varphi\approx\frac{\pi}{2}$. The Coriolis response lies in the $\sin(\omega_1 t-\varphi_1)$ component of $Q_2(t)$. Multiplying Eq. (49) by $\frac{SF}{\mathcal{F}_0\sin(\beta_2-\varphi)}$ gives us the quadrature $\Omega_{z,q}$ and in-phase $\Omega_{z,in}$ errors as

$$\Omega_{z,q}=\left(\frac{m_1^{*}}{4m_c}\right)\frac{\sin(2\psi_2)}{\cos^2(\psi_1-\psi_2)\tan(\beta_2-\varphi)}BW_1$$
$$-\left(\frac{m_2^{*}}{4m_c}\right)\frac{\sin(2\psi_1)\sin(\varphi)}{\cos^2(\psi_1-\psi_2)\sin(\beta_2-\varphi)}BW_2+\frac{\Omega_{z,d}}{\tan(\beta_2-\varphi)},$$

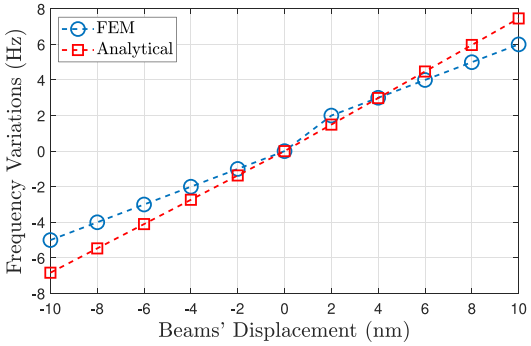

Fig. 12. Frequency variations for different displacements of supporting beams; analytical versus FEM.

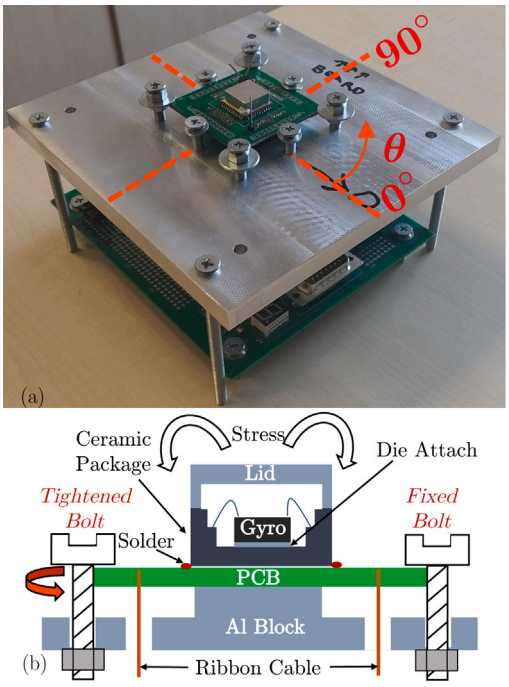

Fig. 13. Stress test setup (a), and concept (b).

$$\Omega_{z,in}=\left(\frac{m_1^{*}}{4m_c}\right)\frac{\sin(2\psi_2)}{\cos^2(\psi_1-\psi_2)}BW_1$$
$$-\left(\frac{m_2^{*}}{4m_c}\right)\frac{\sin(2\psi_1)\cos(\varphi)}{\cos^2(\psi_1-\psi_2)\sin(\beta_2-\varphi)}BW_2+\Omega_{z,d}. \tag{51}$$

- *Mode-mismatched:* $\Delta\omega\neq0$, $\Delta\omega\gg BW_2$, and $\beta_2-\varphi\approx\pi$. The Coriolis response is carried by the $\cos(\omega_1 t-\varphi)$ component of $Q_2(t)$. Multiplying Eq. (49) by $\frac{SF}{\mathcal{F}_0\cos(\beta_2-\varphi)}$ gives us

$$\Omega_{z,q}=-\left(\frac{m_2^{*}}{2m_c}\right)\frac{\sin(2\psi_1)\cos(\varphi)}{\cos^2(\psi_1-\psi_2)\cos(\beta_2-\varphi)}|\Delta\omega|$$
$$+\left(\frac{m_1^{*}}{4m_c}\right)\frac{\sin(2\psi_2)\tan(\beta_2-\varphi)}{\cos^2(\psi_1-\psi_2)}BW_1+\Omega_{z,d}\tan(\beta_2-\varphi),$$
$$\Omega_{z,in}=-\left(\frac{m_2^{*}}{2m_c}\right)\frac{\sin(2\psi_1)\sin(\varphi)}{\cos^2(\psi_1-\psi_2)\cos(\beta_2-\varphi)}|\Delta\omega|$$
$$+\left(\frac{m_1^{*}}{4m_c}\right)\frac{\sin(2\psi_2)}{\cos^2(\psi_1-\psi_2)}BW_1+\Omega_{z,d}. \tag{52}$$

The quadrature and in-phase errors depend on mode shape rotation angles, the demodulation angle, and the sense mode's (mechanical)

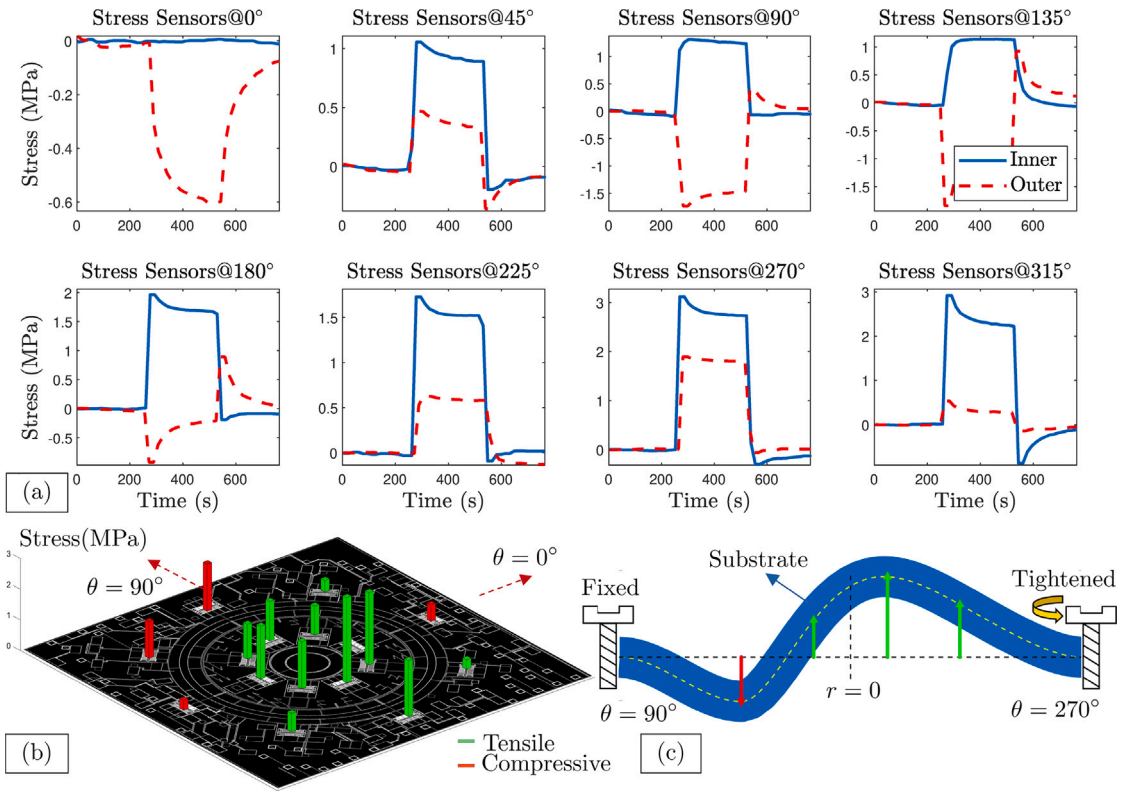

Fig. 14. Stress sensors' outputs during test#1 along 90° (a); maximal stress state's top (b) and (exaggerated) side views (c); inner stress sensor at 0° was nonfunctional.

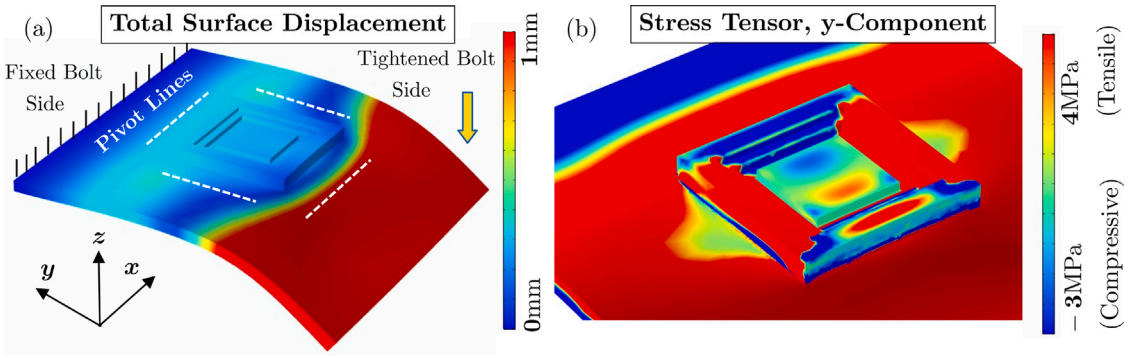

Fig. 15. FEM model of bending along 90° when the bolt and PCB are not centered, generating both tensile and compressive stresses on the MEMS die; displacement profile (a) and stress distribution (b).

phase. As shown by Eqs. (43) and (45), stress can affect all these quantities and induce additional errors.

5. Results and discussion

5.1. Gyroscope specifications

The geometric parameters of the VRG are given in Table 1. We measured the frequencies and quality factors of the drive ($\cos(2\theta)$) and sense ($\sin(2\theta)$) modes as 58.919 kHz, 32.42×10^3 and 58.858 kHz, 31.54×10^3, respectively. The gyroscope has an uncompensated quadrature error of −2125°/s. Using the method proposed in [20], we estimated the mode shape rotation angle to be −2.4°.

5.2. Simulation setup

We built a simulation model in MATLAB that uses the recorded outputs of the stress sensors as the input to interpolate the substrate's strain and displacement fields. The simulation model follows the flowchart in Fig. 10 and implements Eqs. (43), (45), and (52). We replaced the missing data of the nonfunctional stress sensor at 0° by a cubic interpolation of the functioning stress sensors along the $\theta = 0$ axis. We used the first three harmonics $\ell = 1{:}3$ in Eq. (37) as the basis functions for strain interpolation.

5.3. Comparison against FEM

We first assess the accuracy of our model in predicting frequency variations against FEM. For this, we performed a prestressed modal analysis in COMSOL Multiphysics, where all supporting beams undergo the same displacement as visualized in Fig. 2. Fig. 12 shows the comparative graphs; the analytical results have a (least squares) slope of ≈0.7147 Hz/nm, larger than ≈0.5682 Hz/nm of the FEM. This discrepancy is attributable to the analytical model's idealized boundary conditions that lead to higher stiffness estimates. Moreover, in our model, the beams' displacements coincide with the vibration of the

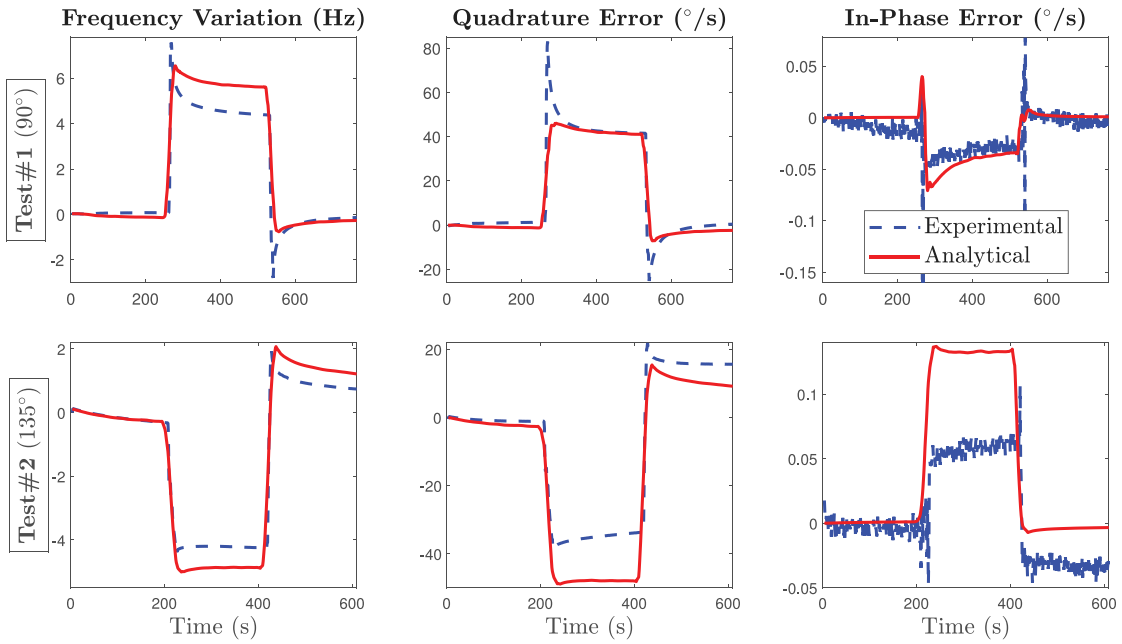

Fig. 16. Variations of drive mode's frequency, quadrature, and in-phase errors during tests#1 and 2; analytical versus experimental.

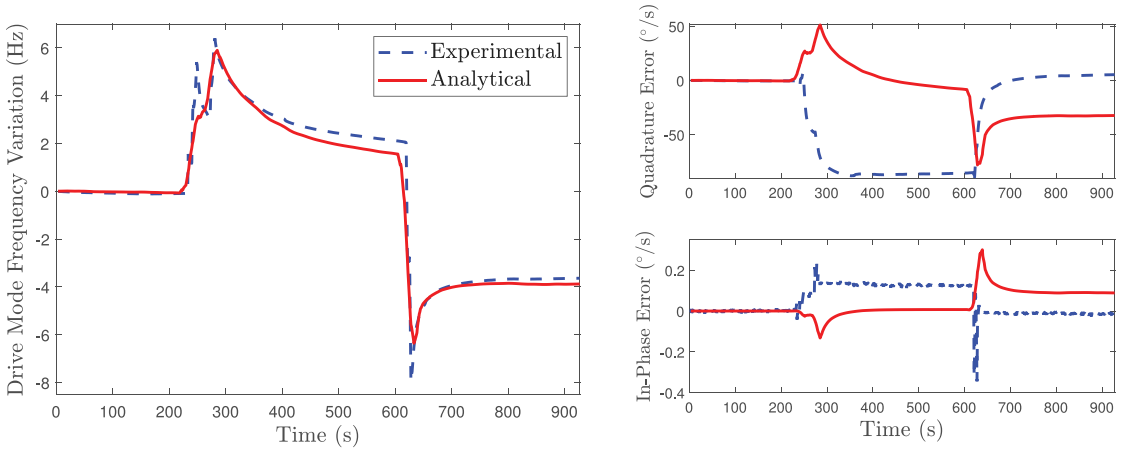

Fig. 17. Analytical versus experimental results for test#3 (0° direction); maximum stress data are missing because of the nonfunctional stress sensor at 0°.

gyroscope, whereas in the prestressed analysis, these displacements precede the vibration.

5.4. Experimental setup

Fig. 13 shows the setup for the stress tests and explains their underlying concept. The gyro PCB is sitting on top of an aluminum block and is held by a set of bolts. By tightening suitable bolts, we can apply bending loads in selected directions. To achieve this, we keep one of the bolts fixed and fasten the bolt on the opposite side. Ribbon cables connect the gyro PCB to a main PCB that acts as the central signal transmission hub for actuation and readouts. We use two 8 × 1 multiplexers as the readout apparatus for the 16 stress sensors such that each stress sensor's output is sampled at every 16 s. The high voltage across the gyroscope's structure was set to 40 V during the tests. Further technical details about the experimental setup can be found in [5].

We performed four tests: test#1 along 90°, test#2 along 135°, test#3 along 0° direction, and test#4 along 90°. During tests#1-3, the device was in the gyro mode, and we recorded the drive mode's frequency, quadrature, and in-phase errors. During test#4, however, the gyroscope was actuated through the sense mode, and we recorded only the frequency. Fig. 14 shows the outputs of the stress sensors during test#1, following the usual sign convention of positive for tensile and negative for compressive stresses. As shown in Fig. 14(b) and (c), the stress is tensile on the tightening side and gradually transitions to compressive on the fixed side. Because we tighten only one of the bolts, the stress profile is not perfectly symmetrical. To further clarify this point, we created a FEM model (Fig. 15(a)) of our system where the MEMS chip is replaced with a silicon block. The bending was applied only in one direction to reflect the practical scenario. There is a hexagonal bolt under the PCB to generate stresses efficiently; however, the daughter board is susceptible to being misplaced and not perfectly centered with the bolt. Fig. 15(b) presents the stress distribution when the PCB and bolt are shifted by 5 mm, which leads to both compressive and tensile stresses on the chip. We remark that the symmetry of the bending profile is not critical for our result, and nonuniform stress distribution helps us better evaluate our model. We also note that the stress sensor located at 0° was nonfunctional (likely short-circuited due to metal routing issues). The maximum stress we observed was around 3 MPa during test#1.

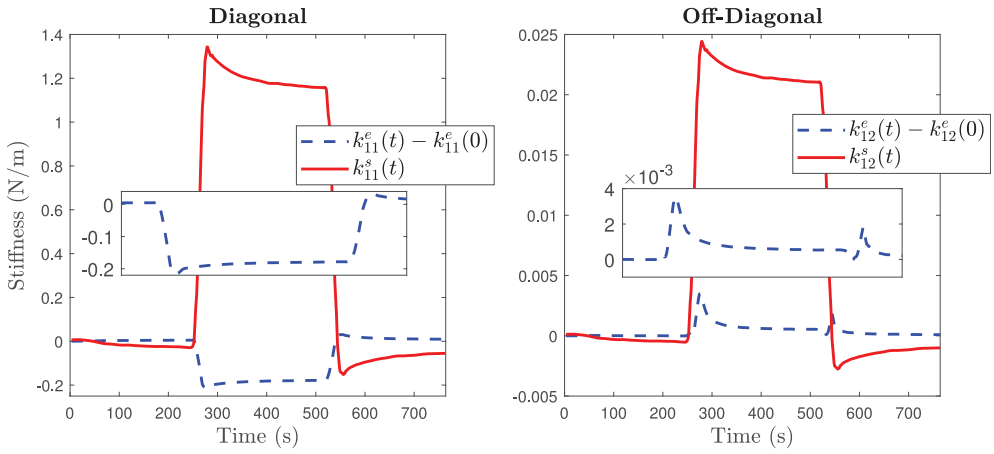

Fig. 18. Stress stiffness (k^s_{ij}) versus variations of electrostatic softening (k^e_{ij}) during test#1.

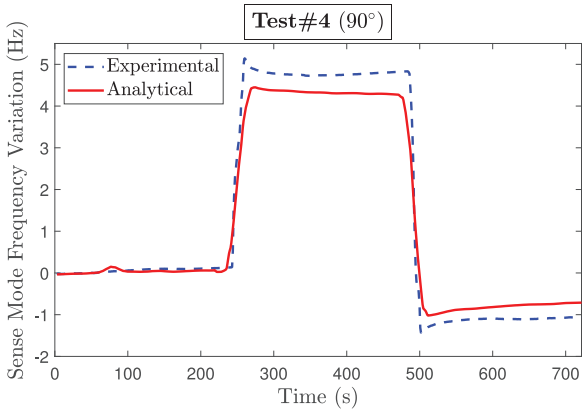

Fig. 19. Sense mode's frequency variation during tests#4; analytical versus experimental.

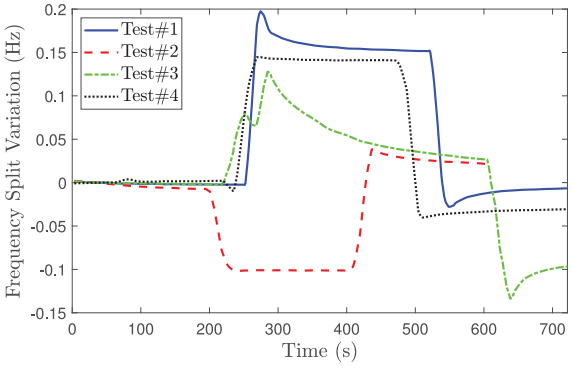

Fig. 20. Predicted variations of frequency split, $\omega_1 - \omega_2$ during stress tests by the analytical model.

5.5. Results

Fig. 16 shows the comparative graphs for the drive mode's frequency variations and quadrature/in-phase errors during tests#1 and 2. The analytical predictions successfully track the corresponding experimental references. We can explain the model's consistency with both increase (test#1) and decrease (test#2) in the frequency by Eq. (32). When there is a net tensile stress distribution, the supporting beams are mostly pushed outward ($\sum_{\ell=1}^{4n} \Delta_\ell(t) > 0$), and we have a hardening effect. On the other hand, a net compressive stress pulls most of the beams inward (e.g., stress relaxation, $\sum_{\ell=1}^{4n} \Delta_\ell(t) < 0$), resulting in a softening effect.

Effect of nonfunctional stress sensors. Accurate interpolation of the substrate's strain is critical for the correct evaluation of stress stiffness. To examine the effect of missing stress sensor data at 0°, we did test#3 along 0° direction so that the maximal stress occurs in the direction of the nonfunctional stress sensor. The results in Fig. 17 suggest that the model still successfully predicts the frequency variation. However, the same does not hold for the quadrature and in-phase errors, implying that the interpolation accuracy is not sufficient to capture the off-diagonal stiffness, δk_{12}.

Stress stiffness versus electrostatic softening. Fig. 18 compares the stress stiffness and variations of the electrostatic softening, as predicted by our model, during test#1. We observe that the stress stiffness dominates the electrostatic softening by several orders of magnitude in both diagonal and off-diagonal entries. We can explain this by noting that, due to the differential arrangement of the electrodes, the anchors on both inner and outer sides have similar displacements. These results accord with the experimental observation in [5] where reducing the high structural voltage from 50 V to 20 V had a negligible effect on the frequency shift.

Sense mode's frequency. According to Remark 2 and Eq. (44), we expect the sense mode's frequency to have a similar level of variation to the drive mode's since $\delta k^*_{11} \approx \delta k^*_{22}$ for small mode shape rotation angles. To validate this point, we conducted test#4 along the 90° direction with the PLL around the sense mode. The stress values during this test were comparable to those of test#1 (maximum stress of 2.5 MPa similar to 3 MPa of test#1). Fig. 19 shows that the sense mode's frequency shifts by about 5 Hz, similar to the drive mode's frequency in test#1.

Frequency split. Based on Eq. (44), Fig. 20 shows that the initial frequency split of 61 Hz is perturbed by≈0.1–0.2 Hz during the stress tests. Variations of frequency split contribute to the scale factor drift, which, according to our analysis, could be calibrated with stress.

Error sources. Based on the presented results, we can categorize the error sources of our modeling as follows.

1. *Errors at the modeling level:* Apart from the approximations inherent in Euler–Bernoulli beam theory, the idealized boundary conditions we assume in deriving our mode shapes and displacement fields tend to produce a *stiffer* model than the actual structure.
2. *Stress measurement errors:* Missing or faulty stress data directly affect the interpolation accuracy, calculated radial displacements of the supporting beams, and the resulting stress stiffness matrix. Our main fabrication-related challenge is the low yield due to process

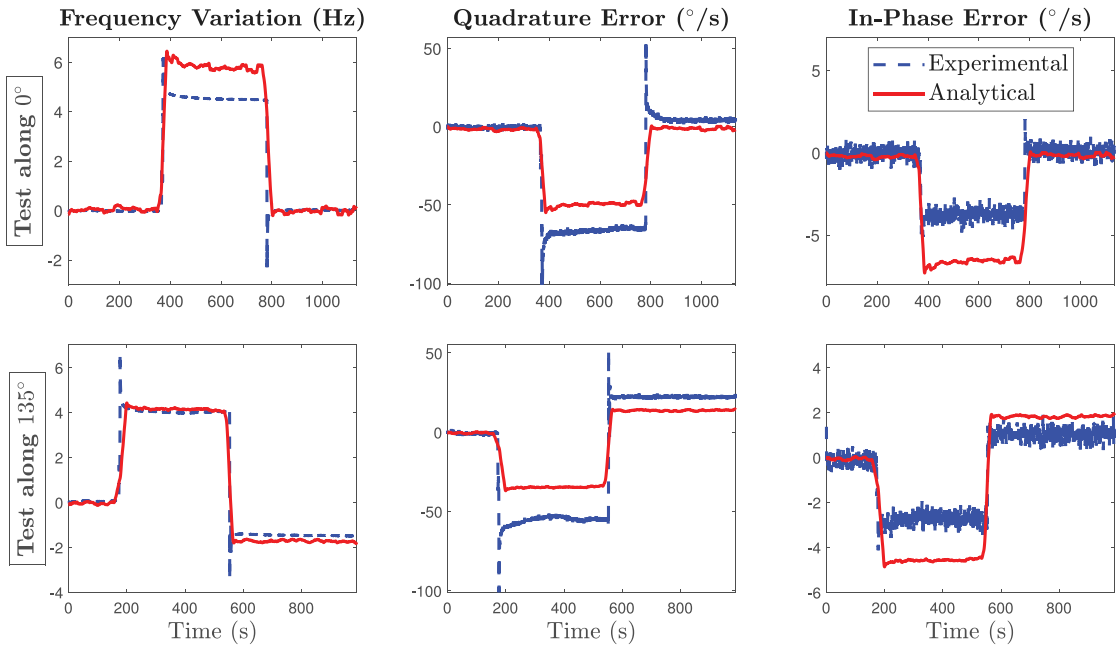

Fig. 21. Analytical versus experimental results for the second gyroscope.

nonidealities, affecting the stress sensors' balance and sensitivity. Overall, stress measurement is the main deciding factor for our model's accuracy.

5.6. Supplementary data

To provide additional supporting data for our modeling, we present partial results from tests done with another 57 kHz, 3.2 mm diameter gyroscope; the frequency data of these results were reported in [6]. As shown in Fig. 21, the level of agreement between the experimental and analytical results parallels the first device. We note that the second gyroscope had four nonfunctional stress sensors at 90° (both inner and outer), 180° (outer), and 225° (inner).

6. Conclusion

We reported a new approach toward understanding the effects of stress in MEMS gyroscopes through analytical modeling. Our model deduces the anchor displacements from the outputs of stress sensors distributed across the gyroscope. Comparison with experimental data demonstrated the efficacy of our model in predicting stress-induced frequency changes and quadrature/in-phase errors. The followings are possible avenues for improving and expanding the results of this paper:

- Incorporating temperature in terms of its effects on material properties and thermomechanical stresses; in our tests, we only dealt with mechanical stresses as the temperature was almost constant (variation < 0.7°C).
- Developing more accurate and, possibly, physics-based strain interpolation methods that are robust against missing or faulty stress data.
- Examining the model's potential for improving the gyroscope's long-term drift performance.

CRediT authorship contribution statement

Mehran Hosseini-Pishrobat: Conceptualization, Methodology, Software, Formal analysis, Writing – original draft, Visualization. **Derin Erkan:** Software, Investigation, Resources, Data curation. **Erdinc Tatar:** Conceptualization, Investigation, Writing – review & editing, Supervision, Funding acquisition.

Data availability

Data will be made available on request.

References

[1] I.P. Prikhodko, A.A. Trusov, A.M. Shkel, Compensation of drifts in high-Q MEMS gyroscopes using temperature self-sensing, Sensors Actuators A 201 (2013) 517–524.
[2] A. Buffoli, P. Segala, M. Gadola, T. Verdot, P. Robert, G. Langfelder, Searching for the origin of zero-rate offset and scale-factor drift in nems-based navgrade gyroscope, in: 2023 IEEE International Symposium on Inertial Sensors and Systems (INERTIAL), 2023, pp. 1–4.
[3] ADIS16488A: Tactical grade, ten degrees of freedom inertial sensor, Technical Datasheet, Analog Devices, 2018, Available URL https://www.analog.com/en/products/adis16488a.html.
[4] E. Tatar, T. Mukherjee, G.K. Fedder, Stress effects and compensation of bias drift in a MEMS vibratory-rate gyroscope, J. Microelectromech. Syst. 26 (3) (2017) 569–579.
[5] B.E. Uzunoglu, D. Erkan, E. Tatar, A ring gyroscope with on-chip capacitive stress compensation, J. Microelectromech. Syst. 31 (5) (2022) 741–752.
[6] M. Hosseini-Pishrobat, B.E. Uzunoglu, E. Tatar, Modeling stress effects on frequencies of a MEMS ring gyroscope, in: 2023 IEEE 36th International Conference on Micro Electro Mechanical Systems (MEMS), IEEE, Munich, Germany, 2023, pp. 869–872.
[7] D.M. Rozelle, The hemispherical resonator gyro: From wineglass to the planets, in: Proc. 19th AAS/AIAA Space Flight Mechanics Meeting, January 2009, Vol. 134, 2009, pp. 1157–1178.
[8] M.W. Putty, A Micromachined Vibrating Ring Gyroscope (Ph.D. thesis), University of Michigan, 1995.
[9] F. Ayazi, K. Najafi, A HARPSS polysilicon vibrating ring gyroscope, J. Microelectromech. Syst. 10 (2) (2001) 169–179.
[10] A.D. Challoner, H.H. Ge, J.Y. Liu, Boeing disc resonator gyroscope, in: 2014 IEEE/ION Position, Location and Navigation Symposium - PLANS 2014, 2014, pp. 504–514.
[11] Y. Xu, Q. Li, P. Wang, Y. Zhang, X. Zhou, L. Yu, X. Wu, D. Xiao, 0.015 Degree-per-hour honeycomb disk resonator gyroscope, IEEE Sens. J. 21 (6) (2021) 7326–7338.
[12] Z. Liu, H. Wen, F. Ayazi, Multi-coefficient eigenmode operation—breaking through 10°/h open-loop bias instability in wideband aluminum nitride piezoelectric BAW gyroscopes, Microsyst. Nanoeng. 9 (1) (2023) 1–11.
[13] J.Y. Cho, S. Singh, J.-K. Woo, G. He, K. Najafi, 0.00016 Deg/$\sqrt{\text{hr}}$ angle random walk (ARW) and 0.0014 deg/hr bias instability (BI) from a 5.2M-Q and 1-cm precision shell integrating (PSI) gyroscope, in: 2020 IEEE International Symposium on Inertial Sensors and Systems (INERTIAL), 2020, pp. 1–4.
[14] G. Langfelder, S. Dellea, F. Zaraga, D. Cucchi, M. Azpeitia Urquia, The dependence of fatigue in microelectromechanical systems on the environment and the industrial packaging, IEEE Trans. Ind. Electron. 59 (12) (2012) 4938–4948.

[15] T. Veske, D. Erkan, E. Tatar, Characterization of packaging stress with a capacitive stress sensor array, in: 2023 IEEE 36th International Conference on Micro Electro Mechanical Systems (MEMS), 2023, pp. 909–912.
[16] S. Schröder, F. Niklaus, A. Nafari, E.R. Westby, A.C. Fischer, G. Stemme, S. Haasl, Stress-minimized packaging of inertial sensors by double-sided bond wire attachment, J. Microelectromech. Syst. 24 (4) (2015) 781–789.
[17] C. Jurgschat, F. Roewer, I. Tóth, T. Ohms, A. Zimmermann, Integrated stress sensors for humidity performance drift analysis and compensation in inertial measurement units, J. Microelectromech. Syst. 31 (6) (2022) 918–926.
[18] B.J. Gallacher, J. Hedley, J.S. Burdess, A.J. Harris, A. Rickard, D.O. King, Electrostatic correction of structural imperfections present in a microring gyroscope, J. Microelectromech. Syst. 14 (2) (2005) 221–234.
[19] S.W. Yoon, S. Lee, K. Najafi, Vibration sensitivity analysis of MEMS vibratory ring gyroscopes, Sensors Actuators A 171 (2) (2011) 163–177.
[20] M. Hosseini-Pishrobat, E. Tatar, Modeling and analysis of a MEMS vibrating ring gyroscope subject to imperfections, J. Microelectromech. Syst. 31 (4) (2022) 546–560.
[21] Z. Ma, X. Chen, X. Jin, Y. Jin, X. Zheng, Z. Jin, Effects of structural dimension variation on the vibration of MEMS ring-based gyroscopes, Micromachines 12 (12) (2021) 1483.
[22] A.A. Barakat, P. Hagedorn, Broadband parametric amplification for micro-ring gyroscopes, Sensors Actuators A 332 (2021) 113130.
[23] W. Mayer, A. Küster, P. Tritschler, T. Hiller, D. Radović, A. Zimmermann, Modeling and experimental analysis of low-cost MEMS gyroscopes under PCB bending stress, in: 2023 IEEE International Symposium on Inertial Sensors and Systems (INERTIAL), 2023, pp. 1–4.
[24] M.M. Torunbalci, S.E. Alper, T. Akin, Advanced MEMS process for wafer level hermetic encapsulation of MEMS devices using SOI cap wafers with vertical feedthroughs, J. Microelectromech. Syst. 24 (3) (2015) 556–564.
[25] C.M. Wang, Y.Y. Zhang, S. Kitipornchai, Vibration of initially stressed micro- and nano-beams, Int. J. Struct. Stab. Dyn. 07 (04) (2007) 555–570.
[26] F. Yang, R. Sedaghati, E. Esmailzadeh, Free in-plane vibration of curved beam structures: A tutorial and the state of the art, J. Vib. Control 24 (12) (2018) 2400–2417.
[27] J.N. Reddy, An Introduction to Continuum Mechanics, second ed., Cambridge University Press, Cambridge, 2013.
[28] C.L. Dym, I.H. Shames, Solid Mechanics: A Variational Approach, Augmented Edition, Springer New York, New York, NY, 2013.
[29] H.-W. Ma, S.-M. Yao, L.-Q. Wang, Z. Zhong, Analysis of the displacement amplification ratio of bridge-type flexure hinge, Sensors Actuators A 132 (2) (2006) 730–736.
[30] G.W. Stewart, J.-g. Sun, Generalized eigenvalue problems, in: Matrix Perturbation Theory, in: Computer science and scientific computing, Academic Press, Boston, 1990.

Mehran Hosseini-Pishrobat received his B.Sc. and M.Sc. degrees in Mechanical Engineering from the University of Tabriz, Iran, in 2013 and 2016, respectively. He is currently a graduate research assistant and Ph.D. candidate at the Department of Electrical and Electronics Engineering, Bilkent University, Turkey. His research interests include the design, analysis, and performance improvement of MEMS sensors with an emphasis on analytical modeling and advanced control/signal processing.

Derin Erkan received the B.Sc. and M.Sc. degrees in Electrical and Electronics Engineering from Bilkent University, Ankara, in 2020 and 2023, respectively. His research interests include analog electronics and microelectromechanical sensors, with an emphasis on vibratory gyroscopes, accelerometers, and acoustic sensors.

Erdinc Tatar was born in Denizli, Turkey in 1985. He received B.S. and M.S. degrees (with high honors) in Electrical and Electronics Engineering from Middle East Technical University (METU), Ankara, Turkey, and Ph.D. degree in Electrical and Computer engineering from Carnegie Mellon University, Pittsburgh, PA, in 2008, 2010, and 2016 respectively.

He was a Graduate Research Assistant with Micro-Electro-Mechanical Systems Research and Applications Center, METU, and with Carnegie Mellon University from 2008 to 2011 and 2012 to 2016, respectively. From 2016 to 2019, he worked as a MEMS Design Engineer responsible for the development of high-performance gyroscopes in Analog Devices, Inc., Wilmington, MA. He has been an assistant professor with the Department of Electrical and Electronics Engineering and National Nanotechnology Research Center (UNAM) in Bilkent University since 2019. His research interests include MEMS sensors with a specific focus on inertial and gas sensors, microfabrication and packaging technologies, and readout and control electronics for MEMS sensors. He is a recipient of the European Research Council (ERC) Starting Grant.